Chapter – 1

INTRODUCTION AND LITERATURE REVIEW

1.1 Introduction

Low carbon steels (C < 0.3 wt%, Table 1.1) of high formability are developed for the line-pipe, automotive, and structural applications, for cost-effectiveness. Conventional low carbon steel (grain size in micron level, i.e., coarse-grained low carbon steel) has low strength leading to increased mass for the automotive applications, which in turn decreases the fuel efficiency [Galan et al. 2012]. The yield strength of these low carbon steels varies between 191 MPa to 247 MPa, and the total elongation varies from 38 to 44% [Kim et al. 1999].

Table 1.1: Various grades of low carbon steel with chemical compositions [Handbook ASM Vol 1. 1990].

SAE-AISI	C wt.%	Mn wt.%	P wt.% Max	S wt.% Max
1005	0.06 max	0.35 max	0.040	0.050
1006	0.08 max	0.25-0.40	0.040	0.050
1008	0.10	0.30-0.50	0.040	0.050
1010	0.08-0.13	0.30-0.60	0.040	0.050

Low carbon steel can be strengthened either by the addition of alloying elements (Mn, Si, Cr, Ti, Nb, etc.) [Handbook ASM Vol 1. 1990], or work hardening or grain refinement or by a combination of some of these methods. Over the last two decades, the development of ultrafine-grained materials has become a top interest of the material researchers due to their attractive, unusual properties for various structural [Valiev et al. 2000]. Among these strengthening methods, grain refinement is the only mechanism which improves strength while maintaining the ductility, if the

grain size is in the micron range [Song et al. 2006]. Therefore, the grain refinement methods are well adapted for strengthening the material. There are two large-scale industrial techniques used for refining the metallic alloys. These are solidification with inoculation and thermomechanical processing. Solidification using inoculants leaves impurities in the material that deteriorate ductility. Thermomechanical processing can produce grain size down to 2-5 μm in the low carbon and low alloy steels [Ueki et al. 1987, Bakkaloğlu 2002, Lee et al. 1995]. Thermomechanical processing ends up in a substantial reduction in cross-section, which limits its application for processing large cross-sections. Low carbon and alloy steel has been rolled upto reduction area 40% at 740°C and results show that, grain size reduced from 18 μm to 8 μm, the yield strength of the steel increased from 330 to 425 MPa, while the ultimate tensile strength increased from 430 to 528 MPa. The elongation decreased from 38% to 27% [Bakkaloğlu 2002]. Panigrahi has rolled a low carbon steel (C-0.018wt%) at 700-650°C up to reduction in area 40%. Results show the grain refinement to 20μm and yield strength 180 MPa and Ultimate strength 310MPa with elongation 41% (Panigrahi 2001).

Recently severe plastic deformation (SPD) methods have been developed to produce ultrafine-grained (UFG) structure in bulk-sized metallic alloys, where the grain size is an order of magnitude lower than those processed by thermomechanical processing or solidification by inoculation process. In these methods, a large amount of shear strain is imposed on the material while constraining the cross-section to remain almost unchanged. The microstructure of the material gets modified due to the incorporation of high density of defects and their progressive rearrangements during continuing strain path.

1.2 Severe Plastic Deformation (SPD) Techniques

Various severe plastic deformation (SPD) techniques have attracted the attention of materials researchers because these techniques are suitable to produce various semi-finished products in the form of sheets, rods, thin foils, bolts and wires [Valiev et al. 2000, Jin et al. 2011, 2012]. SPD techniques can be used to deform the material upto a large plastic strain without any significant change in the cross-section leading to refinement of the microstructure to nano/ultrafine level in the bulk size metals and alloys. A number of SPD techniques were developed in the recent past. These are high-pressure torsion (HPT), Equal channel angular pressing/extrusion (ECAP/ECAE), multi-axial forging (MAF) and multi-axial compression (MAC), Twist Extrusion (TE), accumulative roll bonding (ARB), corrugated groove pressing (CGP), Repetitive corrugation and straightening (RCS), Continuous high-pressure torsion. These processes can be easily employed for severe plastic deformation of bulk materials by making simple modification to existing techniques.

1.2.1 High Pressure Torsion (HPT)

Bridgman et al. [Bridgman et al. 1943] have proposed a technique to deform the solid by torsion combined with compression. In the SPD terminology this method is known as high-pressure torsion. In this technique, a small metal disc of 10-20 mm diameter and 0.1 - 2 mm thickness is deformed by torsion in a constrained die (Figure 1.1) by applying high compressive pressure (usually 1-10 GPa) at room temperature or elevated temperature [Zhilyaev et al. 2001, Sakai et al. 2005, Zhilyaev et al. 2008, Klöden et al. 2009, Song, et al. 2012, Song et al. 2013, Kawasaki et al. 2014, Janecek et al. 2014,]. The disc sample is deformed by surface frictional forces. Shear strain (γ) can be calculated at a distance r from the center of the disc by the following Equation 1.1 [Zhilyaev et al. 2003, Valiev et al. 1996, Wetscher et al. 2004].

$$\gamma = \frac{2\pi Nr}{h} \qquad\qquad (1.1)$$

The equivalent shear strain (or von Mises' equivalent strain) can be calculated by equation (1.2).

$$\varepsilon_{eq} = \frac{\gamma}{\sqrt{3}} \qquad\qquad (1.2)$$

Where N is the number of revolutions, h is the disk thickness. In this process shear strain at rotation axis is zero and it increases with increase in distance from the center (r). In HPT process severity of strain depends upon the number of revolutions of anvil [Zhilyaev et al. 2001, Horita et al. 2005] in the course of friction between the disc-shaped sample and the rotating plunger.
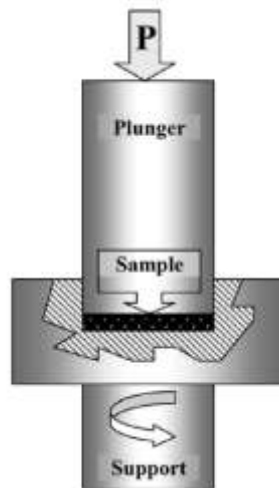

Figure 1.1: Schematic diagram of HPT processing setup [Zhilyaev et al. 2003].

Sakai et al. [Sakai et al. 2005] have reported grain refinement from 0.5 mm to ~200 nm in Al–Mg–Sc alloy by HPT. Therefore, microstructural refinement as well as hardness increases from the center toward periphery of the sample processed by HPT. [Song et al. 2012, 2013, Janeček et al. 2014]. After 5 revolutions the microstructure gets refined to 200-250 nm when the IF steel deformed by HPT and hardness increases from 214 HV at the center to 355 HV at the periphery [Janeček et al. 2014]. Song et al. [Song et al. 2013] have also reported similar results by HPT at

2.5 GPa for 1 revolution; grain refinement to 308 nm and increased in hardness to >350 HV.

1.2.2 Continuous high-pressure torsion (CHPT)

Continuous high-pressure torsion was invented by Edalati et al. in the year 2010. In this technique a 0.6 mm thick and 3 mm wide sheet is torsion strained continuously as shown in Figure 1.2.
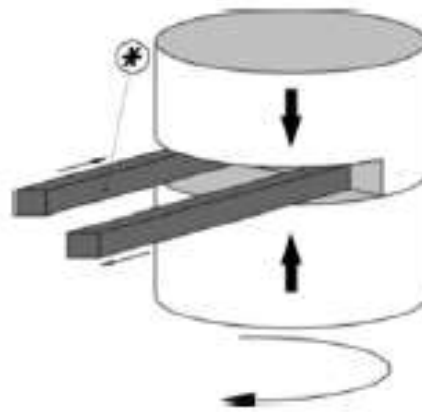

Figure 1.2: Schematic diagram of Continuous high-pressure torsion [Rosochowski et al. 2012].

A high purity Al sample is subjected to continuous high-pressure torsion up to 2 revolutions at 1 GPa pressure and a rotational speed of 1 rpm. Results show that the grain size reduces to 2.1 μm with dislocations in the interior of the grains [Edalati et al. 2010].

1.2.3 Accumulative Roll Bonding (ARB)

Saito et al. invented accumulative roll-bonding (ARB) in the year 1999 at Osaka University Japan [Saito et al. 1999]. ARB is a severe plastic deformation technique by which usually two metals or alloy sheets are stacked and rolled to 50%

of area reduction such that if the two rolled sheets are stacked again and rolled to 50% reduction in area, the method always produces a sheet of an almost initial cross section (Figure 1.3). The rolled sheets are cleaned with a metal brush to remove any foreign material that is detrimental to diffusion bonding. As the cross-section of the rolled sheet remains unchanged, the sheet can be deformed repeatedly. The imposed strains are additive by the repetition of the process and modify the microstructure by enhancing defect density. The amount of imposed strain can be calculated using the following equation 1.3 [Geist et al. 2011].

$$\varepsilon_{eq} = \frac{2N}{\sqrt{3}} \ln\left(\frac{lo}{l}\right) \qquad\qquad (1.3)$$

Where l_o is initial sheet thickness, l is final sheet thickness (after rolling), and N is a number of rolling cycles. Tsuji et al. [Tsuji et al. 2004] have deformed both phosphorus-free and phosphorus strengthened IF steel upto an equivalent strain of 4 by ARB process at 500°C. The former got refined to 0.28μm thickness of the lamellar grain, but in later case, lamellar thickness was reduced to 0.18μm. The steel got strengthened to 750MPa, but the strength of IF steel with phosphorus addition could be increased to 820MPa. Imposing an equivalent strain of 6.4 by ARB on IF steel refines the grain size to 100 nm that increases strength rapidly from 84 MPa to 909 MPa [Jamaati et al. 2015]. Lee et al. [Lee et al. 2004] have reported an increase in strength of IF steel from 280 MPa to 1120 MPa after imposing an equivalent strain of 7.1 using ARB.
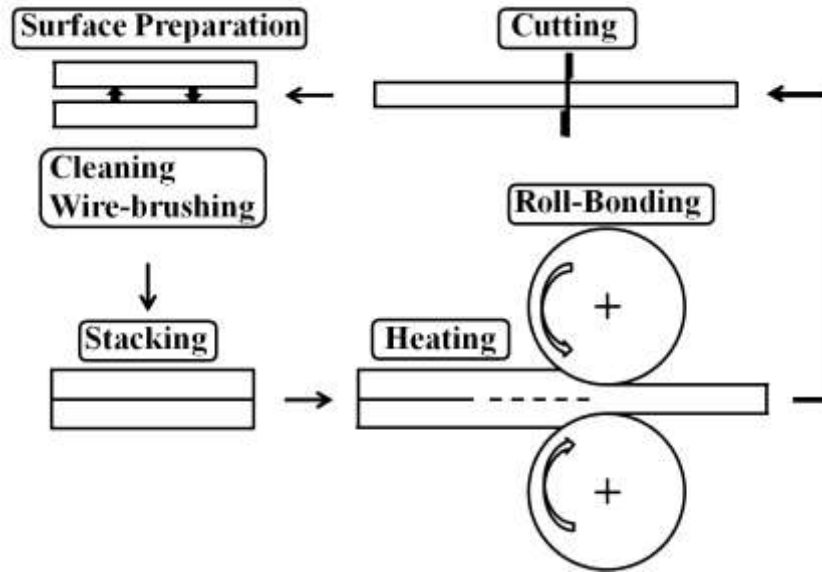
Surface Preparation

Cutting

Cleaning
Wire-brushing

Roll-Bonding

Stacking

Heating

+

+

Figure 1.3: Schematic diagram of accumulative roll bonding process
[Saito et al. 1999].

When an equivalent strain of 8 is applied on IF steel by ARB, the average grain size reduces to UFG (>500 nm) level. Consequently, hardness improves from 98 HV to 247 HV [Tamimi et al. 2014]. Reis et al. [Reis et al. 2005] have also reported the microstructure development in IF steel by ARB up to an equivalent strain of 8. The evolution of microstructure of IF steel during ARB shows that at $\varepsilon_{vm} = 5.6$ grains are get elongated and form the lamellar structure with increased HAGB fraction. As the equivalent strain increases to 6.3, lamellar structure gradually converted into equiaxed structures. Yoda et al. [Yoda et al. 2011] have reported that after application of an equivalent strain of 0.3 on IF steel using ARB process grain size decreases which leads to a reduction in formability (Erichsen value). The process is limited by debonding at surfaces because of insufficient diffusion bonding at low temperature as temperature needs to be restricted to lower level for effective refinement. Therefore the process has limited applicability.

1.2.4 Multi-Directional Forging (MDF)/Multi-Axial Forging (MAF)

Galeyev et al. have introduced multi-directional forging (MDF) as an SPD technique in the 1990s [Galeyev et al. 1990, Salishchev et al. 1995]. In MDF, after every pass of forging, the axis of pressing is changed by 90° (Figure 1.4). MDF works in three orthogonal directions of the sample by repeated settings.
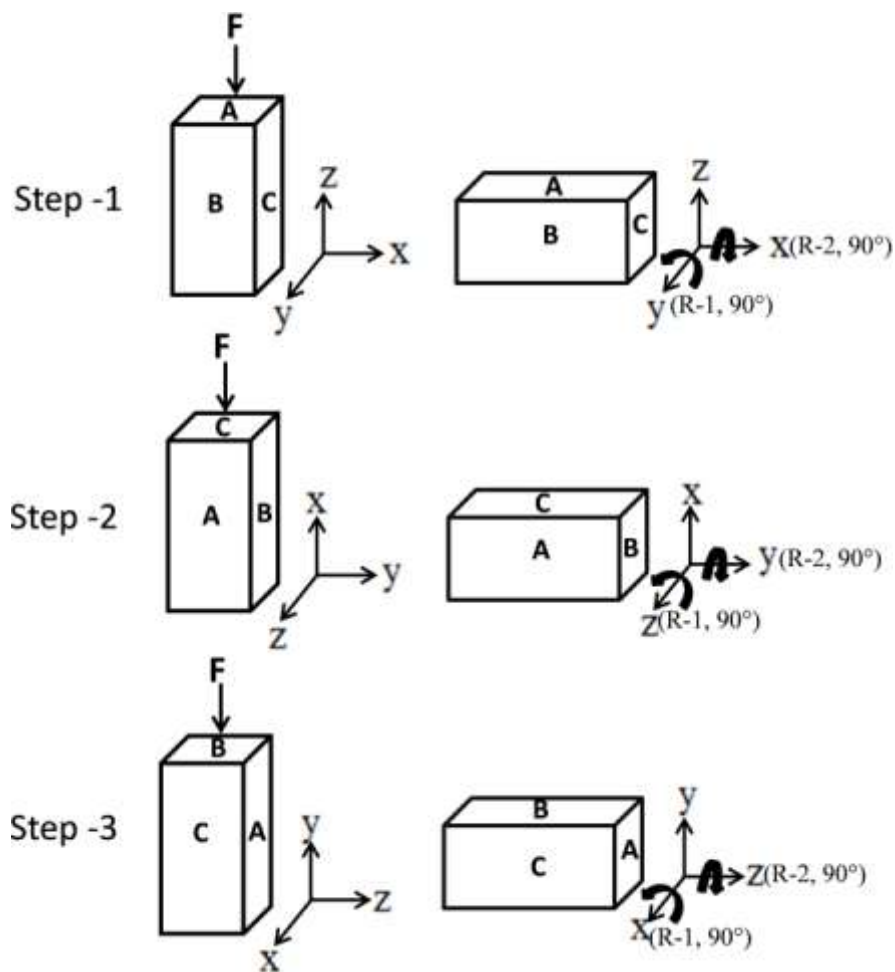

Figure 1.4: Schematic diagram of the multi-directional forging process cycle. The filled black arrows show sample rotation axis.

In MDF process, at the end of the pressing cycle, size of the sample is regained. Therefore a large equivalent strain (ε_{vm}) can be imposed till sample gets fractured (equation 1.4) [Estrin et al. 2013].

$$\varepsilon_{eq} = \frac{2N}{\sqrt{3}} \ln\left(\frac{a}{b}\right) \qquad\qquad (1.4)$$

Where N is the number of cycles, a and b are sample dimensions. Microstructure developed after MDF processing is not as homogeneous as in other popular SPD processes [Estrin et al. 2013].

Zherebtsov et al. have deformed Ti–6Al–4V alloy by MDF technique and successfully applied a total equivalent strain of 3. This resulted in grain refinement to 0.3 μm size, and increase in tensile strength to 1360 MPa with a reduction in elongation to 7% [Zherebtsov et al. 2004]. Soleymani et al. [Soleymani et al. 2012] have imposed an equivalent strain of 2.8 on low carbon steel using MDF and reported grain refinement in ferrite grain size from 38 μm to 1.2 μm. The process led to enhancement in the yield strength from 345 MPa to 850 MPa, ultimate tensile strength from 457 to 1115 MPa, with reduction in total elongation from 25.8 to 7.1%.

1.2.5 Twist Extrusion (TE)

Beygelzimer et al. have brought in a new severe plastic deformation process called twist extrusion first time in the year 1999. [Beygelzimer et al. 1999, Beygelzimer et al. 2002]. In twist extrusion process, a special extrusion die with a twisted channel is used. In this process twisted channel gives the torsion effect and different entry and exit shape of the die introduced extrusion effect on the sample (Figure 1.5). Therefore in this process, deformation takes place by both torsion and extrusion. The sample can be extruded repeatedly by rotating it about extrusion direction by 90° in the clockwise or anticlockwise direction. Therefore a large amount of strain can be imposed without altering the original dimensions of the workpiece. Estrin et al. [Estrin et al. 2013] have calculated the equivalent strain by equation (1.5).

$$\varepsilon_{eq} = \frac{2N}{\sqrt{3}} \tan \gamma \qquad\qquad (1.5)$$

Where N is number passes and γ is the twist line slope. This process can be applied to large-scale billets and production lines, but the drawback of this process is non-uniform deformation in the sample (smallest near the extrusion axis) [Estrin et al. 2013]. Twist extrusion process is less effective in the production of UFG structure as compared with ECAP or HPT [Orlov et al. 2009].
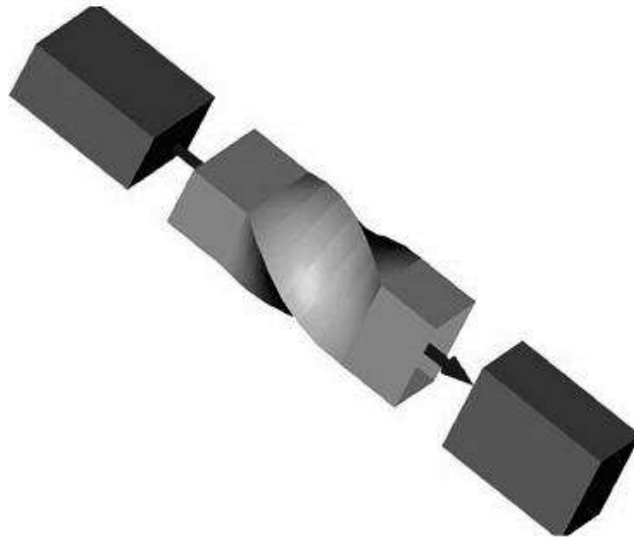

Figure 1.5: Schematic diagram of twist extrusion die with twisted channel and different shape of entry and exit channels of the die with work piece [Beygelzimer et al.2006].

Pashinska et al. [Pashinska et al. 2012] have imposed an equivalent strain of 6 on low carbon steel, and results show that grain size is refined from 15 μm to 5 μm with 84% high angle grain boundaries. Orlov et al. [Orlov et al. 2009] have deformed pure aluminum up to an equivalent strain of 4.8 and reported the strength of 213 MPa and elongation of 38%.

1.2.6 Repetitive corrugation and straightening (RCS)

Repetitive corrugation and straightening (RCS) is an SPD technique by which a plain sheet is sheared through a corrugated die where crests and valleys of two opposite dies plates match with the thickness of the sheet. On compression, the sheet gets a corrugated shape. The corrugated sheet is flattened using a plain constrained die. The flat plate is corrugated again and the process of flattening repeated (Figure 1.6). On completion of one complete cycle, the cross-section of the plate almost remains unchanged, but the shear strain is additive with the number of cycles [Huang et al. 2001, Zhu et al. 2010].
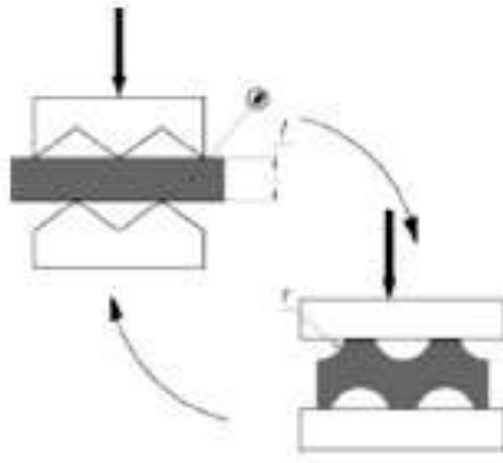

Figure 1.6: Schematic diagram of Repetitive corrugation and straightening (RCS) [Beygelzimer et al. 2000].

The equivalent shear strain imposed in one cycle is given by the following equation 1.6

$$\varepsilon_{eq} = N\frac{4}{\sqrt{3}}\ln\left(\frac{r+t}{r+0.5t}\right) \qquad (1.6)$$

where N is the number of passes in RCS, r is the radius of the semi-circular depressions within the die used to impose the corrugations and t is the thickness of the specimen.

Huang et al. [Huang et al. 2010] have deformed a high purity (99.99%) course-grained (765 μm) copper bar maintained at liquid nitrogen temperature by RCS. After 14 cycles of RCS, course-grained copper refined to 500 nm size, most of the grains are heavily strained and contained high dislocation density.

1.2.7 Equal-channel Angular Pressing (ECAP)

Segal and his co-workers invented the ECAP process in 1977 at an institute in Minsk in the former Soviet Union [Segal patent 1977]. Equal-channel angular pressing (ECAP) is an SPD technique by which metallic alloys are deformed by simple shear deformation through two intersecting channels of equal cross section (Figure 1.7). Every passage of workpiece through die introduces shear strain (γ_1), which can be determined by the following equation 1.7 [Iwahashi et al. 1996].

$$\gamma_1 = \left[2cot\left(\frac{\varphi}{2} + \frac{\Psi}{2}\right) + \Psi cosec\left(\frac{\varphi}{2} + \frac{\Psi}{2}\right) \right] \qquad (1.7)$$

Here ϕ is the inner intersection angle of channels and Ψ is outer arc angle in radians. The imposed strain introduces defects in the material. The interaction of defects and their realignment produce various boundaries and fine-grained structures that intern generate ultrafine-grained microstructure. The process has become popular to produce bulk ultrafine-grained structure in materials [Valiev et al. 1993, 2000, 2006, Valiev 1996, Park et al. 2002, Toth et al. 2014, Wang et al. 2005, Shin[a] et al. 2001]. This technique has the following advantage over other techniques. A more uniform microstructure can be obtained by ECAP. It can be applied to reasonably bulk sized solids of a wide range of metals; from alloys to intermetallics. The technique can be easily adopted at laboratory or pilot plant scale due to low load

required for processing, the material can be processed without picking up impurities [Kim et al. 2001, Valiev et al. 2002, 2006, Fukuda et al. 2002, Park et al 2002, Shin et al. 2005, Song et al. 2006]
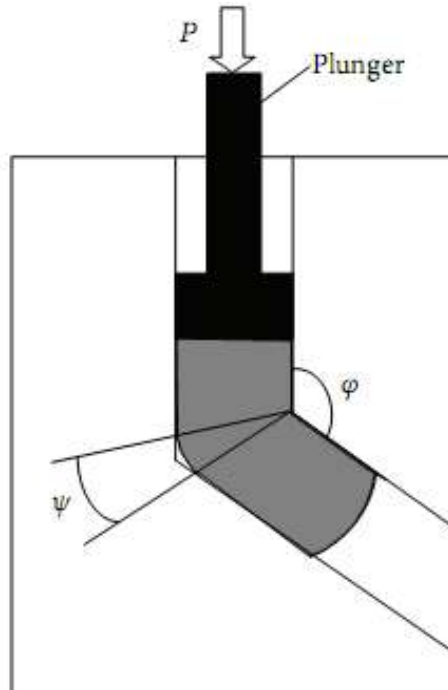

Figure 1.7: Schematic illustration of the equal-channel angular pressing die channel [Azushima et al. 2008].
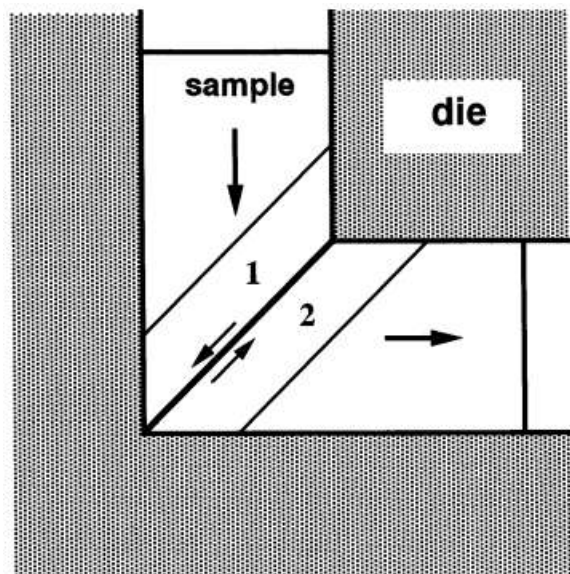

Figure 1.8: The principle of ECAP showing the shearing plane within the die [Nakashima et al. 2000].

In this process, sample passes through the theoretical shear plane as shown in Figure 1.8 and gets deformed. Various parameters like strain per pass, number of passes, pressing speed, processing temperature, process routes, friction between die billet, back pressure, shearing patterns and slip system of material greatly influence the microstructure of the processed material.

a. Influence of Imposed Strain

The imposed shear strain (γ) is additive with number of passes and it can be calculated for N number of passes as given by equation 1.8.

$$\gamma = N\left[2cot\left(\frac{\varphi}{2} + \frac{\Psi}{2}\right) + \Psi cosec\left(\frac{\varphi}{2} + \frac{\Psi}{2}\right)\right] \quad (1.8)$$

Based on equal energy criterion, Von Mises' equivalent strain (ε_{vm}) for N number of passes can be calculated by Equation 1.9 [Iwahashi et al. 1996]

$$\varepsilon_{vm} = \frac{\gamma N}{\sqrt{3}} \quad\quad (1.9)$$

A correlation of equivalent strain with inner intersection angle Φ (from angular range 45 to 180°) and an outer arc angle of Ψ (from angular range 0 to 90°) for a single pass is shown in graphical form in Figure 1.9. From Figure 1.9 an inference can be drawn that lower the die angles Φ and Ψ higher the equivalent strain. Inner intersecting angle Φ has a major effect on the strain imposed during ECAP process [Furuno et al. 2004]. As explained above shear strain for single pass increases with decreasing Φ but decreases with Ψ (Figure 1.9). Increasing shear strain strongly influences microstructural refinement. However, lesser ductile materials require larger Φ value. Therefore, typically Φ is kept utilized in the range of 90°-120° for ductile materials, but for less ductile materials it is used in the range

of 120°-135°. Larger value of Ψ reduce the severity in shear strain, in addition to the incorporation of non-uniformity in deformation at lower zone [Djavanroodi et al. 2012, Basavaraj et al. 2009, Wei et al. 2006, Kim et al. 2004]. The non-uniformity in deformation leads to non-uniformity in texture and in turn to deviations of texture components from their ideal positions [Li[a] at al. 2005, Beyerlein et al. 2009].
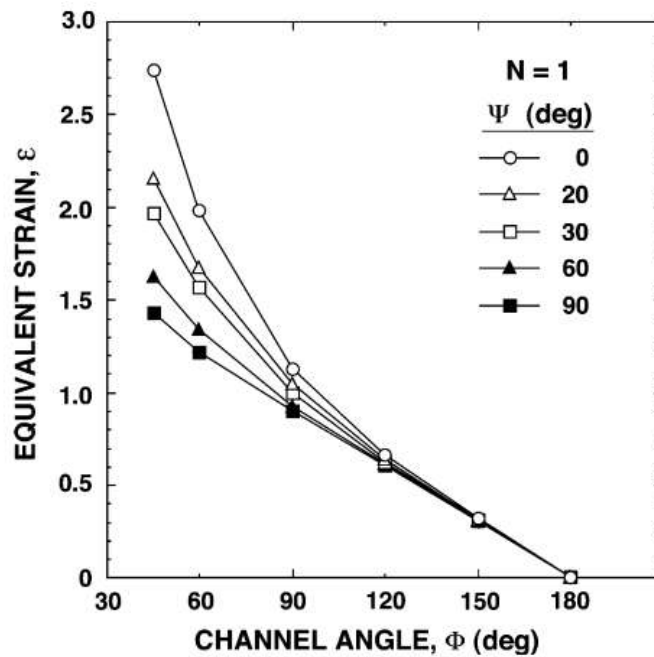

Figure 1.9: Variation of the equivalent strain with the channel angle Φ over angle Ψ [Furuno et al. 2004].

There is a concept of equivalent ratio which is introduced by Segal et al. [Segal 1997, 1999]. It derives the quantity of spent energy adopting route A from the shear strain (γ) imposed by ECAP process and compares to other deformation techniques. These ratios include equivalent extrusion reduction ratio, equivalent rolling reduction ratio etc. The effective or equivalent extrusion reduction ratio ($\lambda_E = f_o/f$) is given by the following Equation (1.10)

$$\lambda_E = e^{\frac{N\gamma_1}{\sqrt{3}}} \qquad (1.10)$$

The effective or equivalent rolling reduction ratio ($\lambda_R = A_o/A$) can be calculated from the following Equation (1.11)

$$\lambda_R = e^{\frac{N\gamma_1}{2}} \qquad (1.11)$$

Where cross-section area reduces in extrusion from f_o to f and rolling reduction in area from A_o to A. γ_1 is the shear strain in a single pass and N is the total number of passes. Changes in the sample parameters like equivalent elongation ratio (λ_l), equivalent aspect ratio (λ_m) and an equivalent thinning ratio (λ_a) can be estimated using the Equation (1.12).

$$\lambda_l = (1 + N^2\gamma_1^2)^{\frac{1}{2}} \qquad (1.12)$$

Equivalent or effective aspect ratio is given by Equation (1.13)

$$\lambda_m = (1 + N^2\gamma_1^2)^{\frac{2}{3}} \qquad (1.13)$$

Equivalent or effective thinning ratio is given by Equation (1.14)

$$\lambda_a = (1 + N^2\gamma_1^2)^2 \qquad (1.14)$$

b. Effect of Routes on ECAP Processing

ECAP process has certain routes to follow during deformation of a regular-shaped sample. Here, routes are classified according to the rotation of the sample between the two consecutive passes of ECAP process. When the orientation of workpiece with respect to its axis remains unchanged between two consecutive passes, the route is designated as A. when sample is rotated by 90° between two consecutive passes, the route is called B. when the sample is rotated about its axis in alternative direction (i.e., clockwise and anticlockwise) between two consecutive passes, the route is designated

as B_A. If the sample is rotated with respect to its axis by 90° always in one direction between two consecutive passes, the route is designated as B_C. However, when the sample is rotated with respect to its axis by 180°, the process is called C (Figure 1.10). In route E sample is ECAPed by route C in two consecutive passes than rotated by 90° and again in next two passes followed by route C. Therefore in route E, two sets of route C are followed (2C X 2C) where after 2C sample is rotated 90° [Barber et al. 2004].
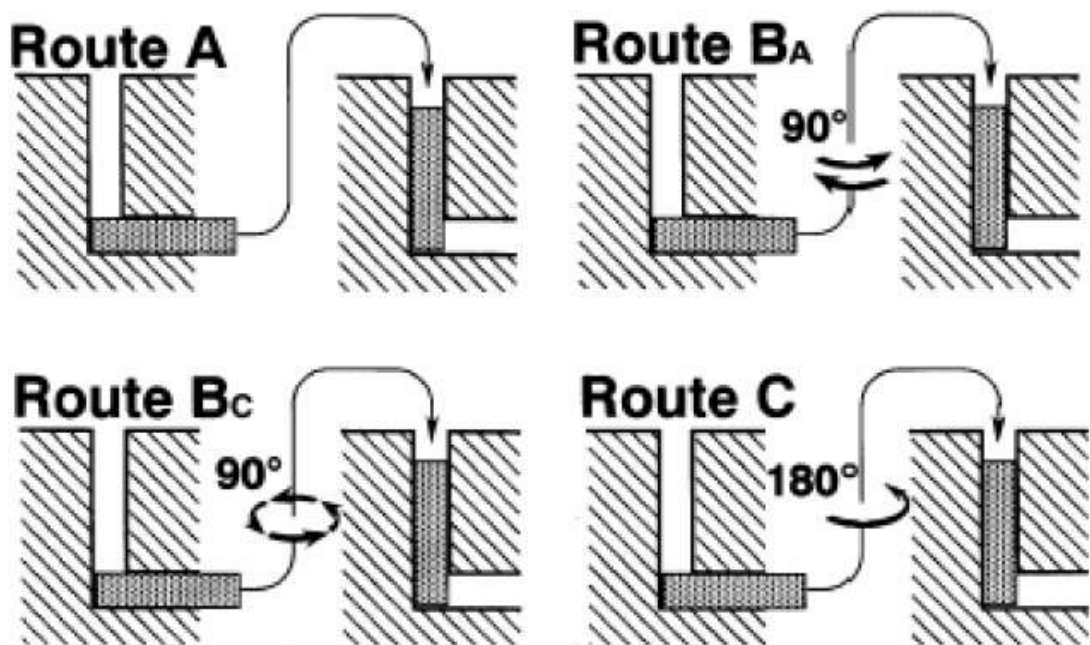

Figure 1.10: ECAP processing routes for multipass deformation [Estrin et al. 2005].

When the material is deformed using route Bc of ECAP process, changes in the shear plane after each pass occur that result in shear banding and instability in the shear plane due to the decrease in stress required for the movement of subsequent dislocations. Moreover, rotation of the sample activates a new set of slip systems which increase the stress required to slip because the DDWs which were already formed, offer obstruction to slip [Rauch 1989, 1992, Prangnell et al. 2004]. In route Bc, isotropic submicron grain structures are formed along with localization of shear

dominated equiaxed submicron grains and undeformed regions [Prangnell et al. 2004]. Grain refinement rate is more in case ECAP of IF steel using route Bc than the other routes [Gazder et al. 2008].

Routes in the ECAP process affect nose and tail (two ends of the billet) of the billet. This effect is maximum for the route A, moderate for the route Bc and minimum for the route C [Agnew et al. 2005]. Cardoso et al. [Cardoso et al. 2011] have compared the effect of route A and Bc on solution heat-treated commercial AA7050 aluminum alloy at 150°C up to 6 passes. In route A, at ε_{vm} = 0.6 (one pass), subgrains are formed with thick walls. The samples processed for three passes (ε_{vm} = 1.8) by route A are having elongated subgrains of 200 nm width. Subgrain width is reduced slightly to 100-200 nm after 6 passes (ε_{vm}=3.6). Whereas in route Bc, the microstructure consists smaller equiaxed subgrains or cells than those obtained in route A. In addition, more dislocations are present at cell boundaries which are independent of the route. Hardness increases after the first pass due to precipitation, microstructure refinement and also from work hardening. Hardness further increases with increasing number of passes (upto ε_{vm}=1.8), thereafter does not vary up to six passes (ε_{vm}=3.6) by route Bc. In route A, the hardness value is similar to the route Bc after one pass (ε_{vm}=0.6) and shows similar hardness even after 6 passes.

c .Shearing Patterns

There are different shearing patterns for different processing routes. In route C, the direction of shear is reversed, and shearing occurs on the same plane between two consecutive passes leading to strain restoration after every even number of passes. On the other hand, in route Bc strain is canceled after every two passes. Route C and Bc can be called as redundant strain processes. The two shearing planes in

route A intersect at an angle of 90°, and four planes intersect at an angle of 120° in route Ba. In this way cumulative increase in additional strain takes place on each separate pass.

Figure 1.11 shows above description on X, Y, Z cubic planes. There is evidence of more severe deformation in case of route A and Ba, whereas restoration of a cubic element after every 2 passes and 4 passes. The cubic element does not get deformed on the Z plane when route A and C are used, whereas nonuniform deformation of X, Y, Z planes takes place using route Ba. Uniform deformation takes place on all planes (X, Y, Z planes) in route Bc at different passes. After a large number of passes, the uniformity in the microstructure of material processed by route B_C is better than that of route A and B_A.

Figure 1.11: The distortions of cubic elements on the X, Y and Z planes of sample for A, B_A, B_C and C processing routes [Furukawa et al. 1998].

Figure 1.12 is showing shearing patterns of Φ=90° and ψ=0° for different routes of ECAP process. In route A, the shearing angle of X and Z planes is zero, but in case of route C, the shearing angle is zero for all the planes (X, Y, and Z). In the route B$_C$, shearing angles in X, Y, and Z planes are 90°, 63°, and 63° respectively after 4 passes of ECAP process.
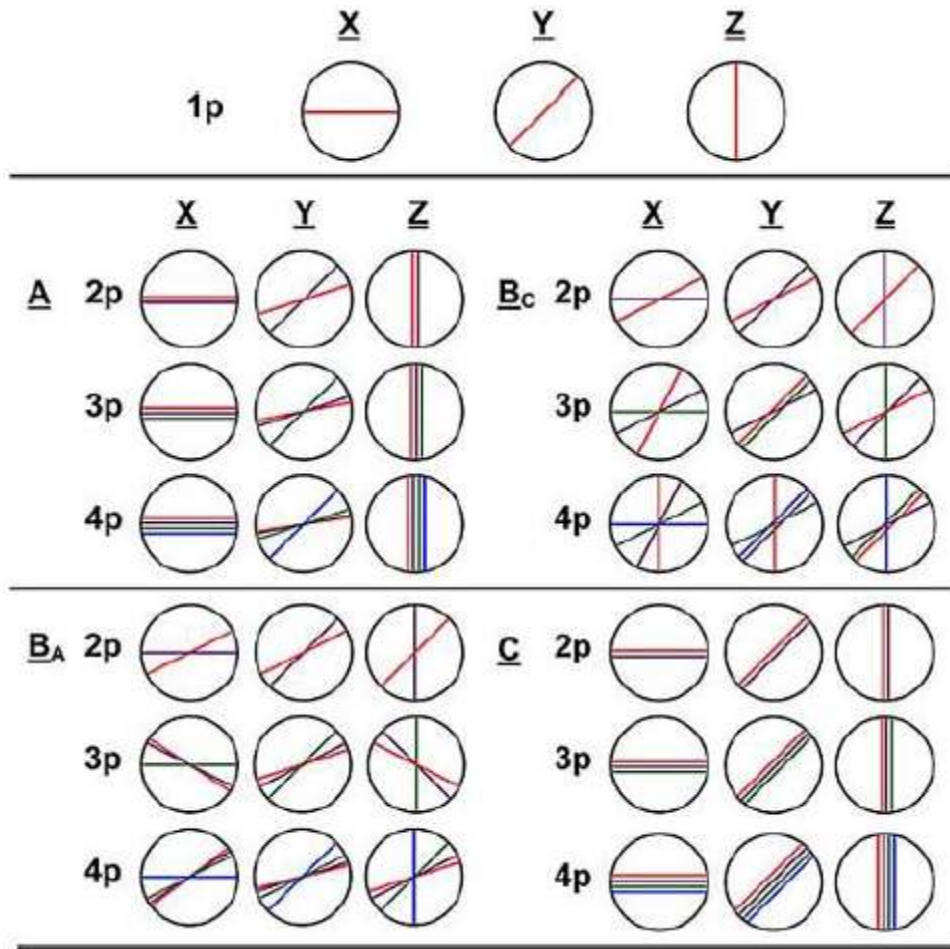

Figure 1.12: Schematic representation of the shearing patterns on the X, Y and Z planes for processing routes A, B$_A$, B$_C$ and C: mauve, green and blue colors correspond to the 1, 2, 3, and 4 pass, respectively [Furukawa et al. 2002].

d. Effect of Pressing Speed, Friction and Back Pressure

At low pressing speed, microstructural changes take place as the part of defects get annihilated at a slow rate but at high pressing speed, the temperature of the sample

increases which lead to dynamic recovery/recrystallisation of the material [Berbon et al. 1999]. When the pressure is applied on the exit side of the sample, it resists cracking and thereby increases workability and facilitates uniformity in metal deformation [Lapovok 2005]. Oh et al. [Oh et al. 2003] have reported that effective strain increases due to application of a back pressing plunger. Djavanroodi et al. [Djavanroodi 2010] have observed a reduction in the dead zone when back pressure is used. Homogeneity of the increases in the sample when the back pressure increases from 50 MPa to 400 MPa [Nejadseyfi et al. 2015]. Back pressure also increases shear zone and uniform material flow [de Barros et al. 2013]. During ECAP process, deformation takes place uniformly at the center of the billet, deformation is less at the front end or nose and back-end or tail. The nose and tail regions are extruded in the billet deformed without back pressure [Oruganti et al. 2005, Bowen[a] et al. 2000] and with increasing number of passes [Rusin et al. 2006, Zhang et al. 2007, Beyerlein et al. 2009]. Friction between billet and die also plays a role as it helps in filling gaps between the sample and die outer corner, top and bottom surfaces of the exit channel but higher friction causes heterogeneous deformation [Oruganti et al. 2005, Bowen[a] et al. 2000]. The friction between the die and billet surface can be minimized by smoothing the sample surface and using lubricants on the surface. These are graphite or molybdenum-di-sulphide dispersed in a liquid medium. Nejadseyfi et al. [Nejadseyfi et al. 2015] have reported that the effect of the back pressure is higher as compared to the ram speed and friction between the die and billet. When the ECAP processing temperature increases load required to deform the material decreases. In ECAP process, for imposing the large strain on the material the sample has to be reinserted many times which leads to increase the processing time and labor. To

overcome this limitation of the ECAP process other methods come into the existence like rotary-die ECAP, side extrusion, parallel channels and multi-pass ECAP.

1.2.8 Rotary-Die ECAP

Rotary-Die ECAP process eliminates the need for removing specimen after each pass. Die contains the two equal-channels intersecting at the center of the die at an angle of 90° (Figure 1.13). In this process sample is inserted in the vertical channel and other three channels punches of equal length are inserted in the opposite ends. One channel out of three channels is free to exit the punch when the pressing is done. Pressing of the sample takes place by applying the pressure on the vertical punch. The die is rotated by 90° after pressing each time, therefore in this process route, A is followed without any rotation.
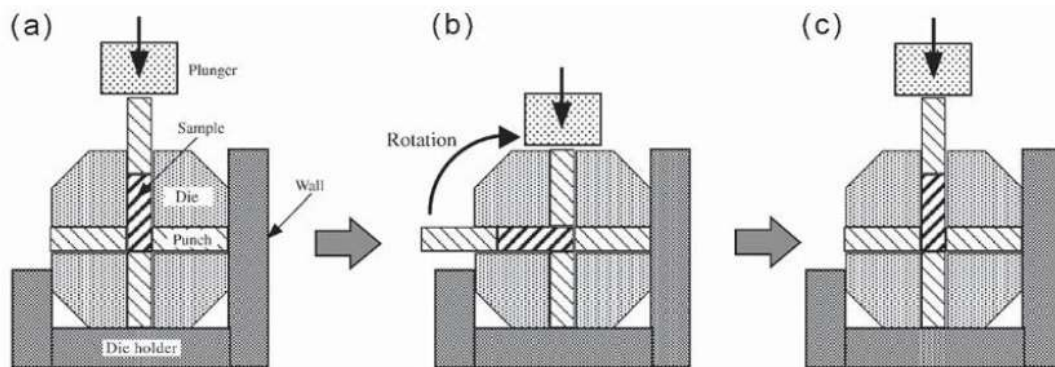

Figure 1.13: Schematic diagram and illustration of operation of Rotary-Die ECAP (a) (initial state) (b) after one pass (c) after 90° die rotation [Valiev et al. 2006].

Hypereutectic Al–23 mass% Si alloy was ECAPed using this technique up to 32 passes at elevated temperature [Ma[a], Ma[b] et al. 2005] and results show that grain got fragmented to less than 150 nm, and Charpy test measured the absorbed energy (13 kJ/m^2) after 32 passes [Ma[a], et al., 2005]. A small aspect ratio of samples is the limitation of this process.

1.2.9 Side Extrusion ECAP

Side extrusion ECAP is also a substitute for regular ECAP process in which high forces are applied by four punch-pull cams (Figure 1.14). In this process, a sample is pressed by punch B and in next pressing by punch A as shown in the figure. 1.12 [Valiev et al. 2006]. In this type of processing pressing route A is followed.
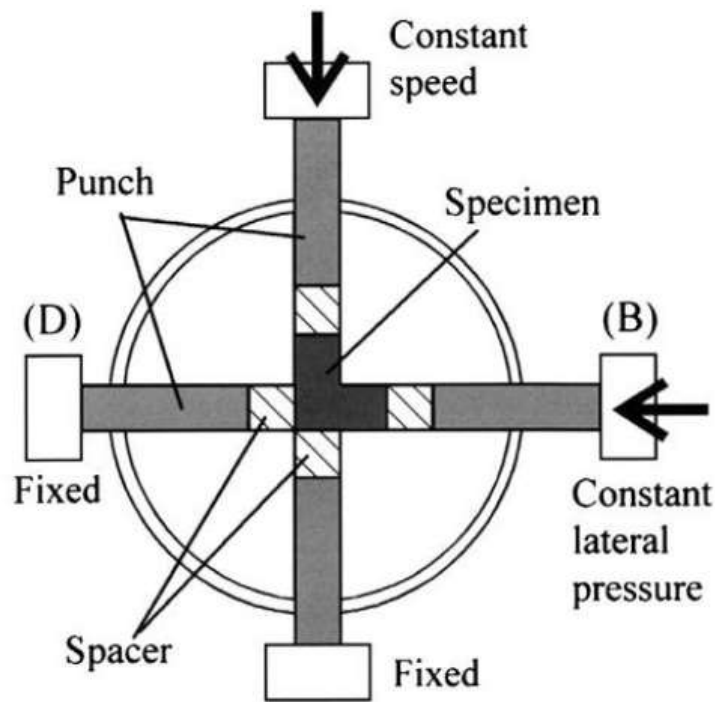

Figure 1.14: Schematic representation of principle of side extrusion process for ECAP [Valiev et al. 2006].

1.2.10 ECAP with Parallel Channel

It is an alternative procedure to impose high equivalent strain in a single pass. Two distinct deformation events take place through two parallel channels to produce ultrafine grains structure in lesser number of reintroduction of the billet. Figure 1.15 shows a schematic illustration of ECAP with parallel channels where Φ is the angle of intersection between channels, K is the distance between two channels, and N shows shearing direction, where shearing plane intersects. Raab et al. [Raab et al. 2005] have

reported the uniform strain distribution in Al sample, including in the tail region, after 8 passes using this process and also reported a grain refinement to 0.6-1.1 μm and increase in strength from 71 MPa to 180 MPa.
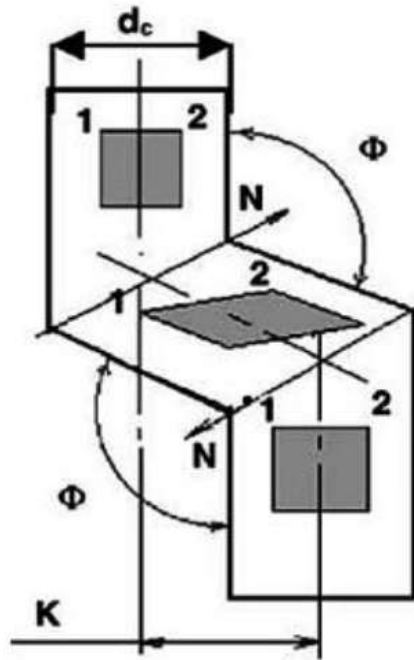

Figure 1.15: Schematic diagram of principle of ECAP with parallel channels
[Raab 2005].

1.2.11 Multi Pass ECAP

Multi-pass ECAP die contains multiple channels constructed at an angle of 90° (Figure 1.16). Route C is followed between two subsequent passes. In the schematic diagram positions 1, 2, 3, 4, and 5 are showing the corresponding pass numbers [Nakashima et al. 2000]. Hwang et al. [Hwang et al. 2015] have deformed low carbon steel using multi-pass ECAE process and reported grain size reduction from 20 μm to 6.7 μm and enhancement in strength from 376 MPa to 718 MPa and elongation from 41.2% to 10%.
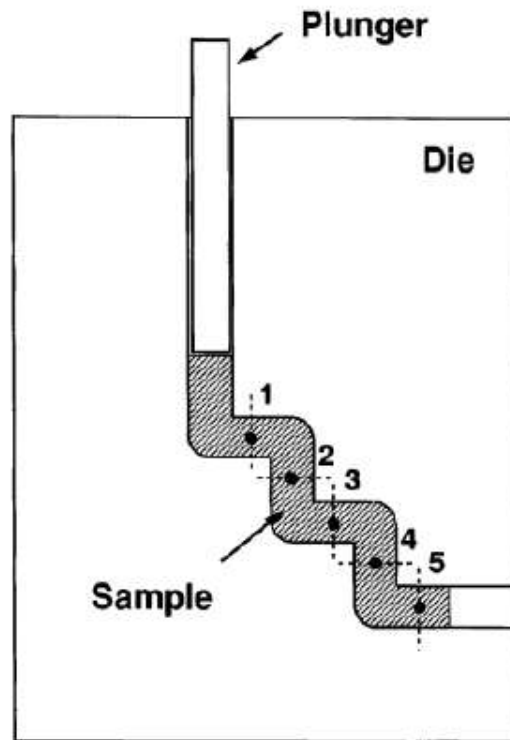
Figure 1.16: Schematic illustration of a multi-pass ECAP die
[Nakashima et al. 2000].

1.2.12 Incremental ECAP (I-ECAP)

Rosochowski and co-authors proposed this technique by extending their knowledge of incremental metal forming techniques, such as swaging or rotary forging, rolling. Here, ECAP is modified it for processing long billets in an increamental fashion [Rosochowski and Olejnik 2011]. The schematic diagram of I-ECAP is shown in Figure 1.17. In this process, deformation takes place by simple shear, similarly to the conventional ECAP. There is no friction force during deformation and consequently reduces the pressing force required is considerably reduced, this enabling processing of large billets.
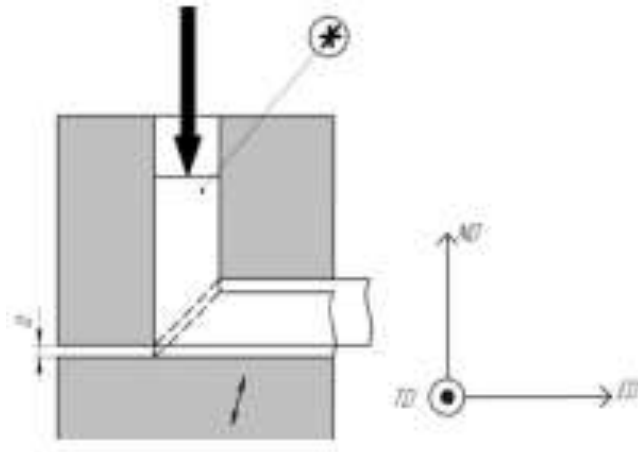
Figure 1.17: Schematic diagram of Incremental ECAP (I-ECAP).

Bars of pure iron, aluminum alloy 5083, CP-titanium and AZ31B with cross-sectional dimensions 10 x 10 mm^2 and length 140 mm were processed by I-ECAP. After 1 pass of I-ECAP at room temperature, the yield strength of pure iron was found to increase from 180 to 490MPa. The material was refined to ultrafine-grain level and Yield strength of Al5083 was increased from 265 to 350MPa after eight passes at 200°C. CP-titanium was subjected to I-ECAP up to 4 passes at 320°C; yield strength was raised from 470 to 805MPa. Four passes of I-ECAP, followed by annealing at 150°C, resulted in a very good combination of strength and ductility in AZ31B magnesium alloy where yield strength was increased from 165 to 305MPa [Gzyl et al. 2016].

1.2.13 Continuous processes (n) ECAP- Conform

About 30 years ago this process was developed for continuous extrusion of wire products [Mizunuma (2006), Alexander (2007)], but in recent times this process has been united with ECAP in the ECAP–Conform process [Tóth et al. 2009]. In this process, with a modified die design was used to generate the frictional force to push a work-piece through an ECAP die as it was used in the Conform process [Mizunuma

(2006)]. Schematic illustration of ECAP–Conform set-up is shown in Figure 1.18 [Tóth et al. 2009].
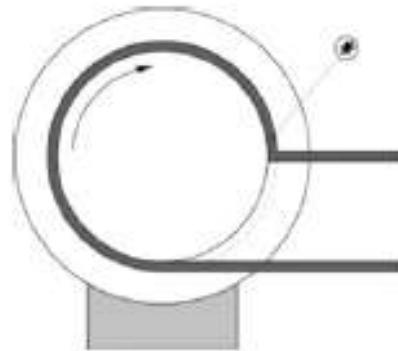

Figure 1.18: Schematic diagram of continuous processes (n) ECAP- Conform [Segal et al. 1994].

A 0.08wt% carbon steel was deformed by this hybrid process. Results showed that UTS increases from 392 to 576 MPa with the elongation of 10% in comparison to the UTS increase of 392 to 523 MPa and elongation of 12.6% when the sample was processed by conventional wire drawing. Thus, the specimen deformed by the hybrid process showed 10.1% higher UTS although elongation was slightly lower when compared to the conventional wire drawing process due possibly to a higher accumulation of strain [Hwang et al. 2011].

1.2.14 Con Shearing

This method was proposed to deform metal strips [Saito et al. 2000, Utsunomiya et al. 2004]. In this deformation technique, the material strip is fed into the mill between satellite rollers and a central roller and all of these rollers rotate at the same peripheral speed to generate a large extrusion force (Figure 1.19). Commercial purity aluminum strips deformed through this technique showed that optimum conditions were achieved for ECAP when the angle within the abutment was set at $\phi = 65°$ [Utsunomiya et al. 2004].
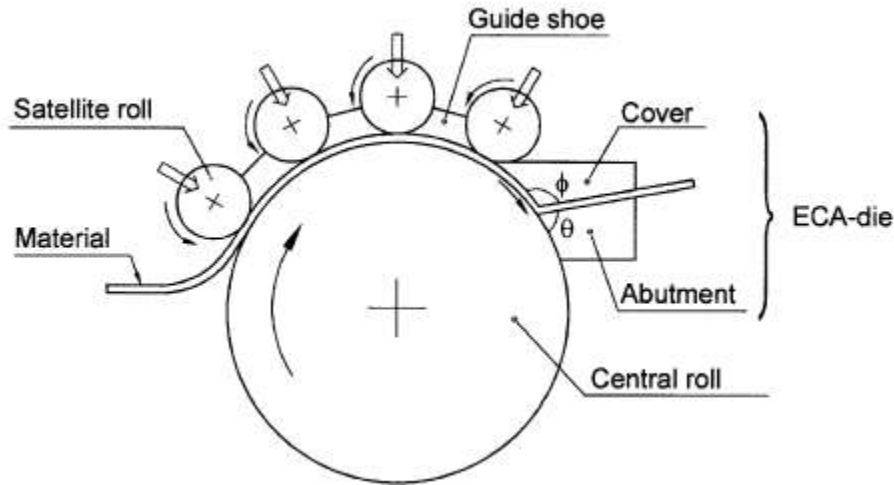
Figure 1.19: Schematic diagram of con shearing process [Raab et al. 2004].

Commercially pure aluminum AA1100 strip 2 mm in thickness, 19 mm in width and 2000 mm in length was deformed by con-shearing process up to 6 passes at room temperature. After four passes, it was observed that approximately 0.5 μm thick banded structure of subgrain has formed. After six passes, the subdivision of the bands to ultra fine grains begins, though the bands remain visible. The mean thickness and the mean length of the grains after six passes are 0.42 μm and 1.44 μm, respectively [Utsunomiya et al. 2004].

1.2.15 Continuous confined strip shearing (C2S2)

In this process, principles of ECAP process were utilized combined with rolling process [Han et al. 2002, Nam et al. 2003].]. The schematic diagram is shown in Figure 1.20.
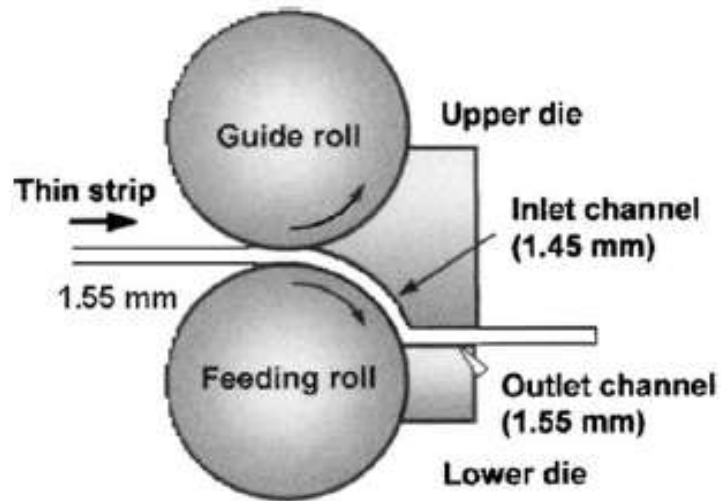
Figure 1.20: The principle of the DCAP process for use in continuous production [Lee et al. 2003].

This process was known with different designations continuous confined strip shearing (C2S2) [Han et al. 2002], dissimilar-channel angular pressing (DCAP) [Nam et al. 2003, Lee et al. 2003, Suh et al. 2003] and equal-channel angular rolling (ECAR) [Nam et al. 2003]. Strips of AA1050 aluminum alloy with the dimension of $1.55 \times 20 \times 1000$ mm were fed into the C2S2 machine with different channel intersection angle in the range of $\phi = 110\text{-}140°$ and deformation cycles up to N=100 ($\varepsilon_{vm} = 58$ at $\phi = 120°$) [Lee et al. 2003]. After the first pass N=1, dislocations begin tangling to form a cell and subgrain structure with high dislocation density in the interior. Misorientation angle was measured to be 3-5°. After N=2 the cell size decreased with increased angle of misorientation. In the range N=2 to 5 though ultrafine grains with high angle boundaries were observed but grain size was increased gradually with increased strain.

1.2.16 Drawbacks of ECAP

The major drawback with the ECAP process and for that matter with all severe plastic deformation techniques is very poor ductility of the processed material. The impressive gain in strength and hardness without any change in dimensions of the starting billet is of little use if the material cannot be further processed mechanically to any desired shape and size. Any attempts by giving conventional thermal treatment to regain ductility would result in considerable loss in strength gained. Second setback of the technique is that the material at the leading and trailing end of the workpiece is not deformed homogeneously as at the center of the billet. Another drawback is that a very large rods cannot be deformed through ECAP because large frictional forces can develop pressure at the entrance channel. Consequently, a high stress is generated on the die, which may fracture at points of stress concentration [Segal et al.1995, Semiatin et al. 1999]. Srinivasan et al. [Srinivasan et al. 2006] have deformed a billet of length 150 mm and 50 mm2 cross-section area using ECAP at the U.S Air Force Research Laboratory (AFRL), which is the largest billet processed by ECAP.

1.3 Post ECAP Deformation

Either cold rolling (room temperature) or cryo-rooling (subzero temperatute) coupled with flash annealing at appropriate temperature following ECAP process can be one such method to regain reasonable amount of ductility at the cost of loosing some strength. Cold rolling and cryo-rolling can further refine the UFG materials, leading to increase in the strength and hardness. During cold rolling of UFG materials, grain refinement takes place due to further deformation, but dynamic recovery annihilates the dislocations generated during deformation [Verma et al. 2017]. Dynamic recovery and recrystallisation are dependent on the rolling

temperature, per pass reduction in the area of rolling, and rolling speed. Cryo-rolling also further refines the UFG materials produced through ECAP. Dynamic recovery and recrystallisation are suppressed due to the low processing temperature. Therefore, the dislocation density is higher after cryo-rolling of ECAPed material as compared to that of cold-rolling. Higher dislocation density achieved in cryo-rolling hinders dislocation movement or leads to the formation of immobile dislocations [Gopi et al. 2012, Chen et al. 2007]. Low work hardening ability of UFG microstructure results from weak interaction with dislocations [Purcek et al. 2012, Wang et al. 2010].

Post ECAP rolling produces sheets with different thicknesses depending on the initial billet size and reduction in area by rolling with improved mechanical properties. These ultrafine grained sheet-metal may be used after some thermal treatment or directly for certain applications.

1.4 Microstructural Development by ECAP

Mechanisms of grain refinement and microstructural modifications through SPD processes are extensively investigated for various metal, and alloys [Prangnell et al. 2004, Hughes 2001, Chang et al. 2000, Furukawa et al. 1998]. During SPD, the grain refinement takes place in the following two steps by; (i) an increase in the dislocation density, the formation of substructure and the cellular structure, and (ii) the conversion of the cellular structure to the granular structure when the dislocation density increases beyond a critical limit [Valiev et al. 2000, Manna et al. 2008].

Prangnell et al. [Prangnell et al. 2004] have deformed Al up to a large strain and reported that at $\varepsilon_{vm} = 2$, coarse grains are subdivided into deformation bands and variety of dislocation structures are formed sequentially, such as the formation of cell blocks within bands containing incidental dislocation boundaries or geometrically

necessary boundaries. At ε_{vm} = 2-4, lamellar structures are formed by aligning boundaries of deformation bands and the already existing high angle grain boundaries (HAGBs) in the direction of deformation. When equivalent strain reaches the range 4-6, the spacing of lamellar boundaries reduces to one or two subgrains-wide. At ε_{vm} = 5, width of lamellar grains further reduces, and elongated bands start taking the shape of a ribbon. At ε_{vm} > 6, inhomogeneous plastic flow induced by texture causes rotation of subgrains leading to breaking of ribbon grains. The rate of grain refinement slows down at higher strain, and ribbon grains get broken down by the formation of transverse low angle grain boundaries (LAGBs). Manna et al. [Manna et al. 2012] have explained the grain refinement mechanisms operative during ECAP of commercial purity aluminum at room temperature. They reported banding of coarse grains at low strain. The grain refinement takes place by rapid rate during this stage. Grains get elongated on further straining (ε_{vm} = 0.6-3.6) through ECAP by simple shear deformation, grains subdivide into bands and subgrain formation in band occurs. Fragmentation of the bands also takes place at the intersection of bands due to rotation of the billet after every pass (ε_{vm} = 1.2-2.4). At-large equivalent strain, the subgrain get converted to grains due to dynamic recrystallisation takes place which leads to conversion of subgrains into grains. Hansen et al. [Hansen et al. 2009] have reported a grain refinement to 90 nm in IF steel using accumulative roll bonding at ε_{vm} = 8. Due to the severity of the strain, several common microstructural characteristics of the non-equilibrium state are often observed. They include the presence of indistinct grain boundaries and a large number of the extrinsic grain boundary. The dislocations in the surrounding area of the grain boundary, i.e., diffused dark lines over a short distance in the vicinity of undefined grain boundary, trapping of the dislocations by the grain boundaries, and the band extinction contours

are observed in many systems [Kornelyuk et al. 1998, Park et al. 2002, Hansen et al. 2001].

Various low carbon steels have been deformed up to a large equivalent strain to attain a microstructural refinement in the range of 200-300 nm [Wang et al. 2005, Shin[a] et al. 2001, Kraus et al. 2011, Fukuda et al. 2002, Maier et al. 2013]. When the low carbon steels are severely deformed through ECAP, a few common features in microstructure are observed owing to the non-equilibrium state of microstructure with ill-defined boundaries. The ill-defined boundaries are also known as high-energy boundaries, and these are the consistent features of severely deformed samples [Wang et al. 2005, Shin et al. 2000].

Wang et al. [Wang et al. 2005] have deformed 0.15%C steel by ECAP adopting route C and found the grains were refined to 0.2 - 0.3 μm at $\varepsilon_{vm} = 10$. The microstructure consists of nearly parallel bands of elongated grains. When a steel with slight lower carbon content exhibited grain size reduction to 0.2 μm from 45 μm when processed via route Bc at $\varepsilon_{vm} = 3$ itself and the microstructure contains elongated subgrains separated by boundaries having low angles of misorientation to nearly equiaxed grains [Fukuda et al. 2002]. Park et al. [Park et al. 2002] have reported similar grain refinement in the case of 0.15wt% carbon steel ECAPed adopting route B_C. (The grain sizes reduces to 0.27 μm and 0.2 μm after $\varepsilon_{vm} = 4$ and $\varepsilon_{vm} = 8$ respectively). ECAP also performed at 350°C up to $\varepsilon_{vm} = 4$ on 0.15wt% C steel. Microstructure is refined to 0.3 μm with severely deformed pearlite [Shin et al. 2005]. While studying the effect of temperature, Kim et al. [Kim et al. 2001] have reported thin parallel shear bands with width 0.2 μm and 0.3 μm in low carbon steel deformed up to $\varepsilon_{vm} = 2$ using ECAP by route A and C respectively at 350°C. Huang et

al. [Huang et al. 2010] have refined IF steel to a grain size of 0.21 μm by accumulative roll bonding process at $\varepsilon v_m = 4.8$.

1.5 Microstructure of Post-ECAP Deformation Condition

Hazra et al. 2010 [Hazra et al. 2011] have reported cold-rolling of IF steel up to a reduction in area of 95% after eight passes ($\varepsilon_{vm} = 9.2$) of ECAP. Results showed that grain boundary spacing reduces from 0.27 μm to 0.08 μm and high angle grain boundary fraction increases to 81%. Verma et al. [Verma et al. 2017] have reported cold-rolling and cryo-rolling of IF steel after 20 passes ($\varepsilon_{vm} = 12$) of ECAP. When the ECAP-12 sample is cold-rolled up to a reduction in area of 90%, the material is dynamically recovered with dislocations rearranged in the form of cells and dislocation tangles. The cell walls of thick dislocation boundaries of 204 nm size are also observed at some places. Most of the cell interiors are dislocation free, and domain size reduces to 34 nm from 41 nm and average misorientation angle increases from 15.8 to 25.9. When the ECAP-12 sample is cryo-rolled up to a reduction in area of 96% at -50°C, a mixture of equiaxed and elongated grain structures are formed. Diffuse grain boundaries are found with grain interior full of large dislocation networks. The grain size reduces from 196 nm to 127 nm with average misorientation angle 25.7°.

1.6 Development of texture in BCC Materials

Deformation reorients crystals due to the presence of easy slip directions in them and it develops preferred orientations which results in texture in materials. Texture is the preferred orientation of the crystals. The orientation of crystal is identified with respect to sample reference axis. An orientation having significant

orientation density is called texture component. Orientation density of a component is presented as a multiple of orientation density of that component in the randomly oriented crystal. A texture component is represented by miller indices of a plane and direction, i.e., (hkl)[uvw], where (hkl is the miller indices of crystal plane whose plane normal is parallel to the normal direction of deformation plane (usually rolling plane) and [uvw] is the crystallographic direction which is parallel to deformation direction(usually rolling direction). The density of orientation of crystal is presented in pole figure as projection of iso density section from density pyramid with respect to sample reference frame (i.e. ND, RD or ED, TD) or sample reference direction (ND, RD or ED, TD) are projected in crystal reference frame as inverse pole figure. The orientation of crystal is also represented by three rotation angles φ_1, Φ, and φ_2 which are called Euler angles and the texture is represented by orientation distribution function in Euler space.

Thus, texture of a material is represented by pole figures (PFs), inverse pole figure (IPFs) and orientation distribution functions (ODFs).

a. Pole Figure

Pole figure is a stereographic projection of poles with density contours on a reference plane. The reference plane is selected based on easily identifiable sample reference direction/plane. Plane normal of a crystal is allowed to intersect to the spherical surface (as shown in Figure 1.21(a) and the intersection point is denoted as the pole. The pole is projected onto a plane whose plane normal is at the center of projection and which is also called as the axis of projection. The same reference frame is true for the deformation directions of the sample. In case of rolled samples, theses are rolling direction (RD), transverse direction (TD), and normal direction (ND) but in

case of ECAPed samples, the corresponding directions are extrusion direction (ED), transverse direction (TD), and normal direction (ND). If a rolled sheet of a single cubic crystal is placed at the center of the sphere as shown in Figure 1.21 (a), the plane of projection is rolling plane, the plane normal is the normal direction (ND), and lies at the center of the projection. Here ND is the axis of projection The poles of (100) planes can be projected on rolling plane as shown in Figure 1.21(b). While a textured polycrystalline material is placed at the center of the sphere its projection of particular poles from each crystal will get clustered on the rolling plane as shown in Figure 1.21(c). The pole density is expressed as the ratio of the number of crystals in the specified orientation to the number of crystals oriented in the specified orientation in a random polycrystalline state of that material. Pole density of particular type of pole is represented in three-dimensions as a pyramid on the projection plane (as shown in Figure 1.21(d)). Pole density of the base of the pyramid is zero and is highest at the peak of the pyramid. The truncated iso density line of the density pyramid is projected on projection plane as isodensity contour line (Figure 1.21(e)). The central contour has the highest density, and outer contour has a lower density. N number of contour lines are projected on projection planes depending on highest orientation density. The texture component is represented by a plane (hkl), and direction [uvw], where hkl are the miller indices of the crystallographic plane which is parallel to rolling plane and [uvw] are the miller indices of crystallographic direction which is parallel to the rolling direction or extrusion direction. A [110] pole figure with directions is shown in Figure 1.22.
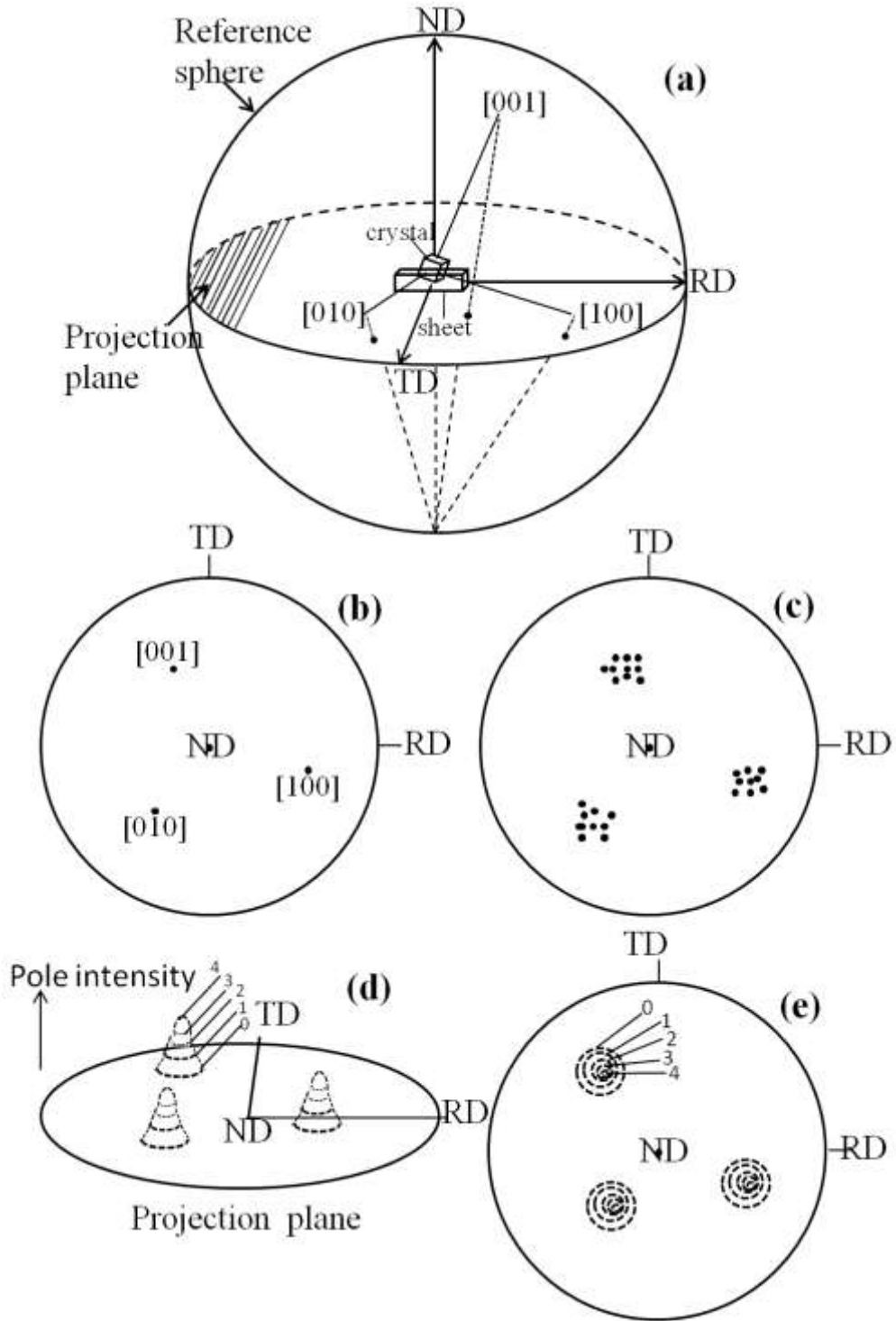
Figure 1.21: (a) Spherical projection of plane normals, (b) projection of poles of single crystal/grain on rolling, (c) projection of poles from textured grains, (d) pole density distribution pyramid, and (e) ND pole figure with pole density contour [Hatherly, and Hutchinson 1979].
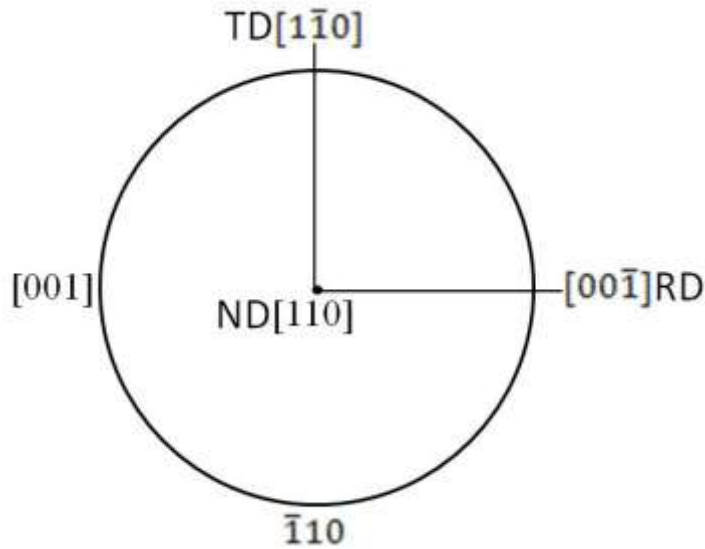
Figure 1.22: [110] pole figure of rolled BCC material.

b. Inverse Pole Figure

Inverse pole figure gives iso density contours of deformation directions projected on crystal reference frame. Inverse pole figure is the representation of texture where sample reference directions (ND, TD, and RD) are projected on crystal reference frame. Therefore there are three types of IPFs, i.e., ND [001], TD [010], and RD [100]. Figures 1.23(a-c) give the inverse pole figure maps of ND, RD, and TD of bcc steel.
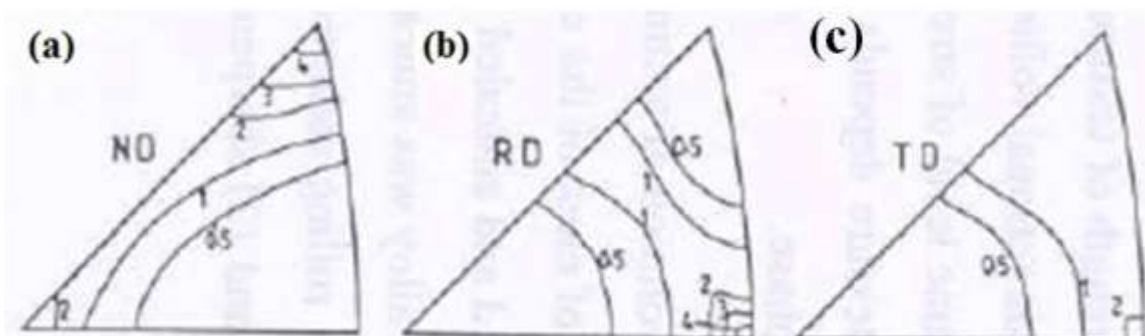

Figure 1.23: Inverse pole figure for 70% cold rolled steel: (a) ND, (b) RD and (c) TD [Hatherly, and Hutchinson 1979].

c. Orientation distribution function (ODF)

The crystal orientation can also be specified by three Eulers angles (φ_1, Φ, φ_2). If X[100], Y[010], and Z[001] are three perpendicular crystallographic axis and A[RD], B[TD], and C[ND] are three perpendicular sample reference directions then Euler angle φ_1 is the rotation angle of crystal around Z such that X becomes parallel to AB, Euler angle Φ is the rotation angle of the crystal around X such that Z becomes parallel to C and Euler angle φ_2 is the rotation angle of crystal around Z such that X becomes parallel to A, Y becomes parallel to B and Z become parallel to C (Figure 1.24).
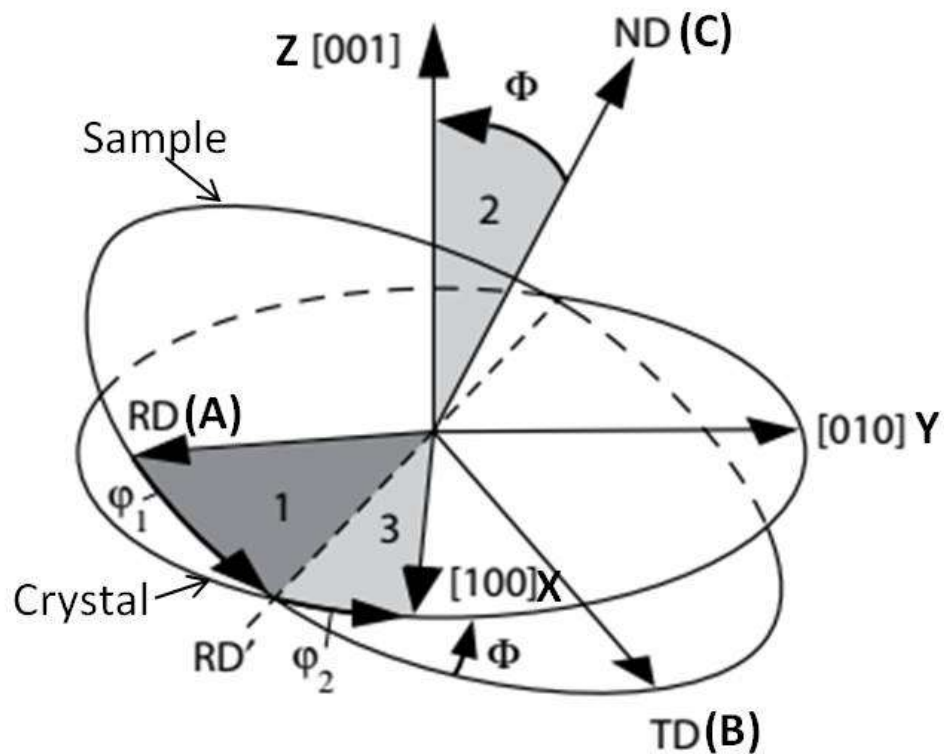

Figure 1.24: Schematic representation of Euler angles φ_1, Φ, and φ_2 [Engler et al. 2009].

The orientation distribution function (ODF) is the distribution of orientation density of polycrystalline material in a 3D space (called Euler space) specified by three Euler angles (φ_1, Φ, φ_2) arranged in three perpendicular directions (Figure 1.25(a)).

In general, the angles range over $0°<\varphi_1<360°$, $0°<\Phi<180°$, and $0°<\varphi_2<360°$. In rolled bcc materials major texture components are available within $\varphi_1=90°$, $\Phi=90°$ and $\varphi_2=90°$, therefore Eulers space is normally drawn within the cube limited by 90° of all three angles. In the Eulers space, every point indicates an orientation (hkl)[uvw] and the orientation density is the strength of texture component in x-random unit. Every density is denoted in three dimensional space in color and equal density contour shows up as a colored surface in the 3D Euler space. As the orientation density is difficult to visualise in 3D ODF the orientation distribution is displayed on a φ_2 section of 3D ODF as projected iso density contours truncated from density pyramid (Figure 1.25(b)).
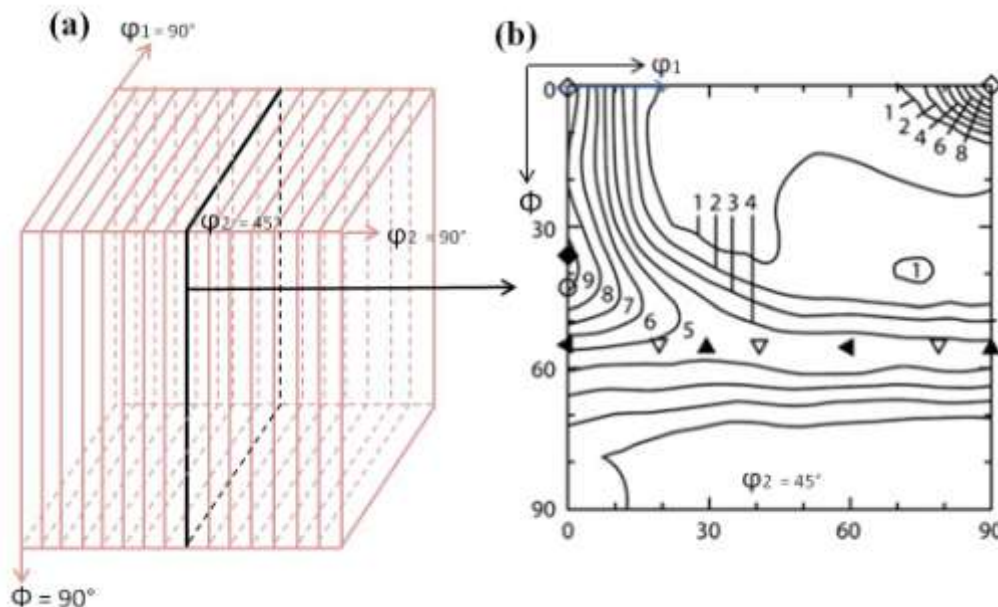

Figure 1.25: (a) Schematic diagram of Euler's space for BCC material, and (b) 2D-orientation distribution Function (ODF) map of Ti-Nb IF steel at $\varphi_2=45°$ [Urabe et al. 1994].

In rolled bcc materials major texture components are available within $\varphi_1=90^o$, $\Phi=90^o$ and $\varphi_2=90^o$.

The ODF g of grains is given by equation 2.11.

$$ODF\ (g) = \frac{1}{V} \frac{dV(g)}{dg} \qquad\qquad (2.11)$$

Where, V is the total texture volume and dV(g) is change in the texture volume with change in orientation.

Texture develops in steel by various processes like pure shear deformation by rolling or recrystallisation during annealing treatment and simple shear deformation during equal-channel angular pressing.

1.6.1 Rolling Texture

Pure shear texture in BCC material consists at least four active slip systems [Haldar et al. 2009]. It exhibits orthotropic symmetry [Bolmaro et al. 1992]. Most of the work on the deformation textures of BCC metals and alloys has been concentrated on low and extra low carbon steels [Ray et al. 1990, 1994] in deep drawing stage of cold rolled and recrystallized form. For deep drawing applications, which require a higher degree of plastic flow in the plane and resistance to flow in the thickness direction of the sheet, it is necessary to optimize texture. Ideal rolling texture components of BCC material are shown in the Table 1.2, Figure 1.26(a). The deformed BCC material shows fiber texture rather than individual components. Location of major fibres are shown in Figure 1.26(b).

Table 1.2: Texture fibers in rolled BCC materials

Fiber	Orientations	Orientation Range
α-fiber	⟨110⟩ ∥ RD	{001}⟨110⟩ to {111}⟨110⟩
γ-fiber	⟨111⟩ ∥ ND	{111}⟨110⟩ to {111}⟨112⟩
η-fiber	⟨001⟩ ∥ RD	{001}⟨100⟩ to {011}⟨100⟩
ε-fiber	⟨110⟩ ∥ TD	{001}⟨110⟩ to {111}⟨112⟩
ζ-fiber	⟨110⟩ ∥ ND	{011}⟨100⟩ to {0$\bar{1}$1}⟨110⟩

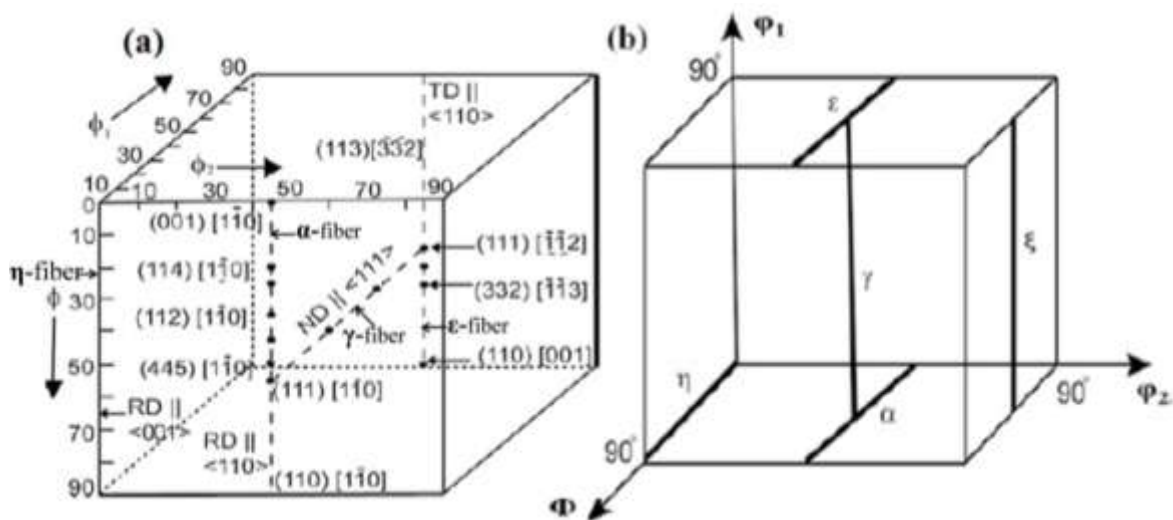**Figure 1.26:** (a) Locations in Euler space of the ideal orientations of BCC materials and (b) Schematic ODF and important fiber locations produced by rolling, RD, ND, TD, denote the three main fibre lines for which rolling, normal and transverse directions are parallel to the ⟨110⟩, ⟨111⟩, and ⟨110⟩ crystallographic vectors respectively [Toth et al. 1990].

The ideal components for rolling texture are shown in Table 1.3.

Table 1.3: Main ideal orientations in rolling texture of bcc materials [Suwas et al. 2008].

Texture component	Eulers Angles (°)		
{hkl}⟨uvw⟩	ϕ_1	ϕ	ϕ_2
{011}⟨110⟩	45	0	0
{211}⟨011⟩	51	66	63
{111}⟨011⟩	60	55	45
{111}⟨112⟩	90	55	45
{11,11,8}⟨4,4,11⟩	90	63	45
{11,11,8}⟨110⟩	0	90	45

The rolling of bcc metals is described by two main fiber textures (Figure 1.22): (1) partial α-fiber with <110> ∥ rolling direction and (2) γ-fiber with <111>∥ normal direction [Kohler et al. 1995]. Both of these fibers are observed in $\varphi_2 = 45°$ ODF section of Figure 1.27. Somjeet et al. [Somjeet et al. 2009] have reported that stronger rolling texture is formed by more homogeneous deformation of the fine-grained microstructure. The less random grains in the hot bands rotate towards a more stable orientation during rolling. Rotation of grains is reported to have such paths of crystal rotation   {110}< 001 >→{554}< 225 >→{111}< 112 >→{111}< 110 >→{223}< 110 > [Inagak et al 1994].

ND and TD denote the three main fiber lines for which rolling, normal, and transverse directions are parallel to ⟨110⟩, ⟨111⟩, and ⟨110⟩ crystallographic vectors, respectively [Toth et al. 1990].

Urabe et al. have reported the strongest component of the cold-rolling texture at {112}<110> after 70% reduction and perceptible shift to the {223}<110> location after 85% cold rolling [Urabe et al. 1994].
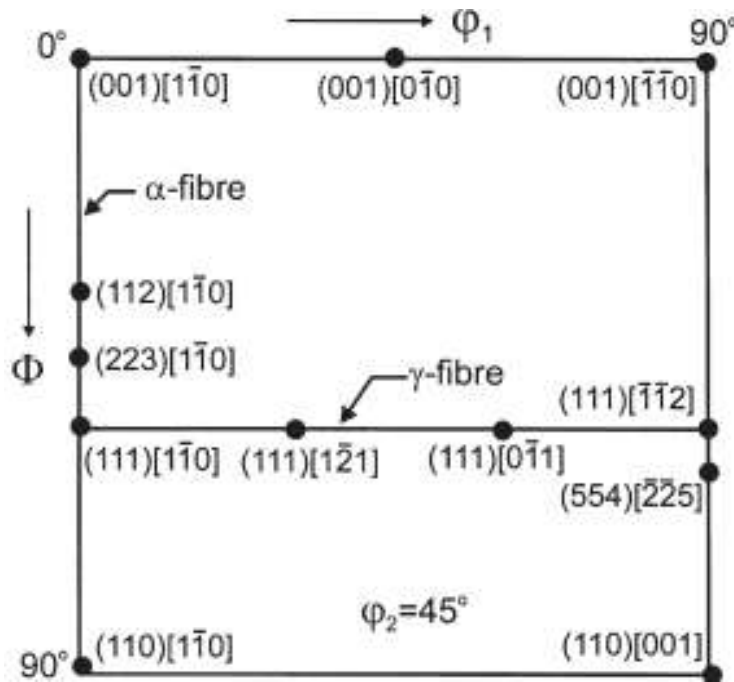
Figure 1.27: 2D ODF of rolled BCC material $\varphi_2 = 45°$ [Humphreys et al. 1995, Hutchinson 1999].

1.6.2 Recrystallisation Texture

When heavily deformed material is annealed, a strong recrystallisation texture is formed which involves preservation of deformation texture. On annealing, the nucleation of new grains takes place with a large number of orientations, but the migration rate of grain boundaries of the new grains of specific orientations is much greater than others which results in recrystallisation texture.

In low carbon steel, the new grains, whose {111} planes are parallel to the rolling plane, grow rapidly and develop {111} components [Ray et al. 1994]. The growth of new grains of these specific orientations leads to recrystallisation texture. In many cases, formation of a different and strong new texture after deformation is also found [Doherty et al. 1997]. There are two proposed models for the formation of a strong new texture, viz., oriented nucleation and oriented growth [Doherty et al. 1988]. Hatherly has reported that the only orientations that are available to a nucleus

during recrystallisation are those present in the deformed material [Hatherly 1990]. Kesten et al. have cold-rolled and annealed low carbon steel and found that dominant recrystallisation mechanism was selective growth acting on a high stored energy nucleation texture. The selective growth mechanism has been characterized by the increased mobility of grain boundaries containing 32° <110> and 38° <111> misorientations [Kesten et al. 1996]. Inagaki has reported the formation of {111} recrystallized grains in the grain boundary region of the {111} deformed grains through the subgrain growth mechanism in the cold-rolled followed by annealed low carbon steel [Inagaki 1994].

The components of the fiber change as deformation texture transforms to recrystallisation texture. The desirable texture for good ductility is γ fiber, i.e., orientation of maximum fraction of grains having {111} planes parallel to the deformation plane or slip plane [Haldar et al. 2009, Ray et al.1994, He 2013].

1.6.3 Simple Shear Texture

The shear texture was first introduced by inhomogeneous rolling at a very high rate of reductions on the subsurface layer of a sheet of Al [Hölscher et al. 1994]. In simple shear texture, there is the two-fold axis in the center or lower symmetry. It can also be described as rotated or sheared texture concerning pure shear texture and contains a wide spread of background intensity. The simple shear texture is weaker than pure shear texture at same equivalent strain level [Bolmaro et al. 1992]. There are only two active slip systems needed in the simple shear deformation to develop ideal orientations [Haldar et al. 2009].

The main ideal orientations and fiber textures in simple shear of BCC materials are shown in Table I.4.

Table 1.4: Ideal orientations in simple shear of BCC materials [Beyerlein et al. 2005, Li[a] et al. 2005].

Sr.No.	Components	{hkl}<uvw>	φ_1, (°)	Φ, (°)	φ_2, (°)
1	$D_{1\theta}$	$(\bar{1}\bar{1}2)[111]$	54.74/234.74 144.74	45 90	0/90 45
2	$D_{2\theta}$	$(11\bar{2})[111]$	125.26 35.26/215.26	45 90	0/90 45
3	E_θ	$(110)[1\bar{1}1]$	90	35.26	45
4	$\bar{E}_\theta$	$(\bar{1}\bar{1}0)[\bar{1}1\bar{1}]$	270	35.26	45
5	J_θ	$(110)[1\bar{1}2]$	90/210	54.74	45
6	$\bar{J}_\theta$	$(\bar{1}\bar{1}0)[\bar{1}12]$	30/150/270	54.74	45
7	F_θ	$(110)[001]$	0/180 90/270	45 90	0/90 45

The Figure 1.28 shows pole figure containing ideal components for negative simple shear deformation. It contains partial <111> fiber (denoted as $<111>_\theta$) and {110} fiber (denoted as $\{110\}_\theta$) that are CCW (counter clock-wise) rotated around transverse direction (TD) for $\theta \sim 60°$ die having major intersection angle of $\Phi=120°$. $<111>_\theta$ fiber contains $D_{1\theta}/D_{2\theta}$, $E_\theta/\bar{E}_\theta$ texture components and the $\{110\}_\theta$ fiber contains $E_\theta/\bar{E}_\theta$, $J_\theta/\bar{J}_\theta$ and F_θ components [Li[a] et al. 2005]. Simple shear texture formed during ECAP process is rotated around TD axis and is an axis of symmetry in simple shear process.
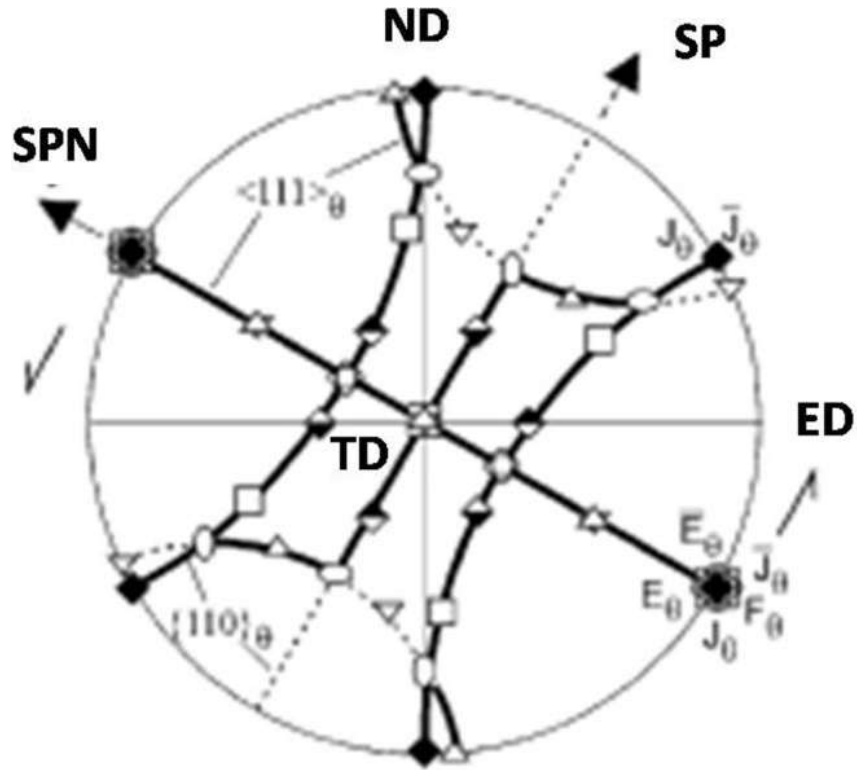
Figure 1.28: [110] pole figure showing the locations of the corresponding main ideal orientations ($D_{1\theta}$, $D_{2\theta}$, E_θ /$\bar{E}_\theta$, J_θ/$\bar{J}_\theta$, and F_θ) and fiber textures (<111>$_\theta$ and {110}$_\theta$) derived from negative simple shear by a 60∘ CCW-rotation around the z-axis. Contour levels:1/1.4/2/2.8/4/5.6 [Li[a] et al. 2005].

Simple shear deformation by ECAP develops texture significantly [Toth et al. 2004, Zhilyaev et al. 2006, Li[a] et al. 2005, Beyerlein et al. 2009]. Texture evolution is dependent on initial texture of material [Ferrasse et al. 2004, Li[b] et al. 2006], friction between workpiece and die [Zhilyaev et al. 2006, Li[b] et al, 2005], strain paths or processing routes [Suwas et al. 2009, Li et al. 2007, Ferrasse et al. 2004, Li[b] et al. 2006], channel intersection angle of die [Li[a] et al. 2005], sharpness of intersection of channels [Zhilyaev et al. 2006, Li et al. 2007], slip systems of materials [Li[a] et al. 2005], microstructural components and amount of strain applied [Toth et al. 2004, Kang et al. 2010, Ferrasse et al. 2004]. Jining et al. [Jining et al. 2005] have also reported temperature effect on the shear texture. Initial strong texture has an influence on texture development of aluminum alloy at initial passes (1-3), and its effect is

maximum for route C compared to route A, B (Ba), C and D(Bc) [Ferrasse et al. 2004]. Heterogeneous deformation induced by friction especially at the bottom of the die develops heterogeneity in texture [Li[a] et al. 2005, Beyerlein et al. 2009]. In case of ECAP by route A or C, texture symmetry is maintained for cubic materials for large number of passes as long as deformation remains homogeneous in the sample depending on the type of materials [Gholinia et al. 2000, Li[a] et al. 2006, Gazder et al. 2006, Ferrasse et al. 2004]. In other routes BA, Bc texture is rotated in other than texture symmetry axis (TD), and symmetry is lost just after the first pass. Therefore texture is strongly dependant on number of passes or equivalent strain and its prediction becomes difficult [Li[b] et al. 2005]. It is, thus, necessary to determine texture at every strain level in the large equivalent strain range.

Inner intersection angle shifts the ideal components by half the difference in intersection angle about TD [Manna et al. 2012, Li[a] et al. 2005, Gazder et al. 2006]. By the lowering of intersection angle, the ideal components become stronger for the same number of passes. Relative intensities also get affected, and some of the components vanish, but some new components also appear [Pereloma et al. 2005, Gazder et al. 2006]. Non-zero outer arc angle ψ leads to non-uniform deformation. Material at lower zone remains undeformed by simple shear but the top layer gets more deformed and the effective strain in the central layer is reduced. This non-uniformity in deformation leads to texture non-uniformity and deviation of texture components from their ideal position. However, the texture gradient and deviation are strong functions of strain path and amount of strain [Li[b] et al. 2006, Tidu et al. 2000, Isaenkova et al. 2005, Bhowmik et al. 2009]. Li et al. have explained the correlation between the texture developed after ECAP single pass and texture in simple shear in bcc material [Li[a] et al. 2005]. ECAP single pass texture components can be correlated

by rotating texture components by φ/2 in negative simple shear about the normal direction of the sample to match with the ideal components of simple shear [Li et al. 2007].

When the deformation takes place through slip under tension or compression, the crystal lattice rotates so that the active slip direction gets aligned with the direction of the applied stress [Hu 1974]. Grains of certain crystallographic orientations are developed due to rotation of grains into stable orientation during simple shear in macroscopic shear plane and direction. There are numerous studies characterizing microstructure and simple shear texture development in ECAP process at low equivalent strain level in low carbon steel. Kang et al. have deformed low carbon steel up to $\varepsilon_{vm} = 2$ and reported weakening of simple shear texture with an increase in the shear strain having $\langle 110 \rangle \| TD$ and $\{111\} \| ND$ along with a high fraction of high angle boundaries [Kang et al. 2010]. Verma[a] et al. have reported texture evolution in IF steel from low to high strain ($\varepsilon_{vm} = 24$) using route Bc. At low strain ($\varepsilon_{vm} = 0.6$), J_θ and $\bar{J}_\theta$ components along the $\{110\}_\theta$ fiber and E_θ, $\bar{E}_\theta$ along $\langle 111 \rangle_\theta$ fiber are existing, but their intensities are low and are away from their ideal positions. As the strain increases to intermediate level ($\varepsilon_{vm} = 1.8\text{-}6$), J_θ, $\bar{J}_\theta$, $D_{1\theta}$ and $D_{2\theta}$ components get intensified. At high strain range ($\varepsilon_{vm} = 9\text{-}24$), high-intensity $\langle 111 \rangle_\theta$ fiber components $D_{1\theta}$ and $D_{2\theta}$ are formed near their ideal position [Verma[a] et al. 2016].

Preferred orientation or texture plays an important role in strengthening, work hardening, formability, and fracture behavior of the material. Deformation at high strain level dissolves part of the second phase specially carbides that strongly influence microstructure of steel [Ivanisenko et al. 2003, Li et al. 2011, Shin et al. 2003]. As the prediction of the texture components in ECAPed material that had undergone ECAP processing adopting route B_C are different due to rotation of texture

around a non-symmetric axis, texture components need to be determined experimentally. The relationship between specific texture components and microstructural features including dissolution of carbides in the low carbon steel ECAPed at low to high strain level adopting route Bc need to be addressed.

1.7 Mechanical Properties of Ultrafine-Grained Materials

Enhancement of strength and hardness takes place in manyfold in comparison to conventional coarse-grained material when the steel is subjected to ECAP processing [Kim et al. 2001, Valiev et al. 2002, Fukuda et al. 2002, Song et al. 2006]. The ductility is maintained in the specific combination of phases while they are in ultrafine size range [Park et al. 2005]. Usually, ductility goes down in the single-phase ultrafine-grained material produced by severe plastic deformation but if microstructure is tailored to a bimodal grain-size distribution ductility can be recovered while retaining high strength to a reasonable extent [Wang et al. 2002, Song et al. 2006]. Ultrafine-grained metals/alloys produced by SPD fail by brittle fracture with decreasing grain size, but the fracture behavior changes to a mixture of ductile & brittle nature when the microstructure gets refined to submicron levels [Verma[b] et al. 2016].

Different strain levels lead to different mechanisms to operate such as grain boundary diffusion, sliding or intragranular deformation which are also responsible for a variety of mechanical properties [Valiev 2013]. Valiev et al. have reported the potential applications of SPD nanostructured materials in the automobile (piston cylinder) aerospace, medical devices (high strength fasteners), sports products (golf stick) [Valiev et al. 2006]. Various UFG materials processing techniques are

developing for economical and continuous production [Raab et al. 2004, R.Z. Valiev 2006, Lowe 2006,].

1.7.1 Strengthening behavior of ultrafine-grained material

Equal-channel angular pressing of 0.2 %C steel for $\varepsilon_{vm} = 4$ by route C at 623° K, results in reduction of grain size to 0.2 μm and increase in ultimate tensile strength (UTS) from 400 MPa to 970 MPa [Shin[a] et al. 2001]. Evenwhen carbon content is lower i.e., 0.15wt.% C steel the reported increase in UTS is close to 950 MPa [Shin et al. 2003] (Table 1.5). The same 0.15 wt.% C steel exhibited UTS >1200 MPa and grain refinement to 0.2-0.3 μm even though it was processed at room temperature for a maximum imposed strain of 10 [Wang et al. 2005]. A 0.1wt.% C steel has been ECAPed for an equivalent strain of 3 via route Bc at 150°C which results in an increase in tensile strength from 307 MPa to 824 MPa due to grain refinement to 0.3-0.6 μm [Kraus et al. 2011]. Fukuda et al. [Fukuda et al. 2002] have reported that ECAP of 0.08wt.% C steel for $\varepsilon_{vm} = 4$ via route Bc at room temperature refines the grain size to 0.2 μm and improves UTS from ~350 MPa to > 800 MPa

Strengthening behavior of IF steel at low to high equivalent strain level by ECAP is given in the Figure 1.29 [Verma[b] et al. 2016]. At a lower equivalent strain of 0.6, strength increases rapidly to 560 MPa due to the grain refinement to 0.39 μm and high dislocation density. As the imposed equivalent strain increases from 1.8 to 3, strengthening rate decreases due to the recovery process and a decrease in grain refinement rate. At ε_{vm} range 9 - 24, a decrease in grain size and the increase in misorientation angle together overcome softening due to the earlier mentioned recovery process; thereby strengthening takes place at a constant rate. At $\varepsilon_{vm} = 24$, grain size reduces to 0.25 μm and strength increases to 937 MPa [Verma[b] et al. 2016].
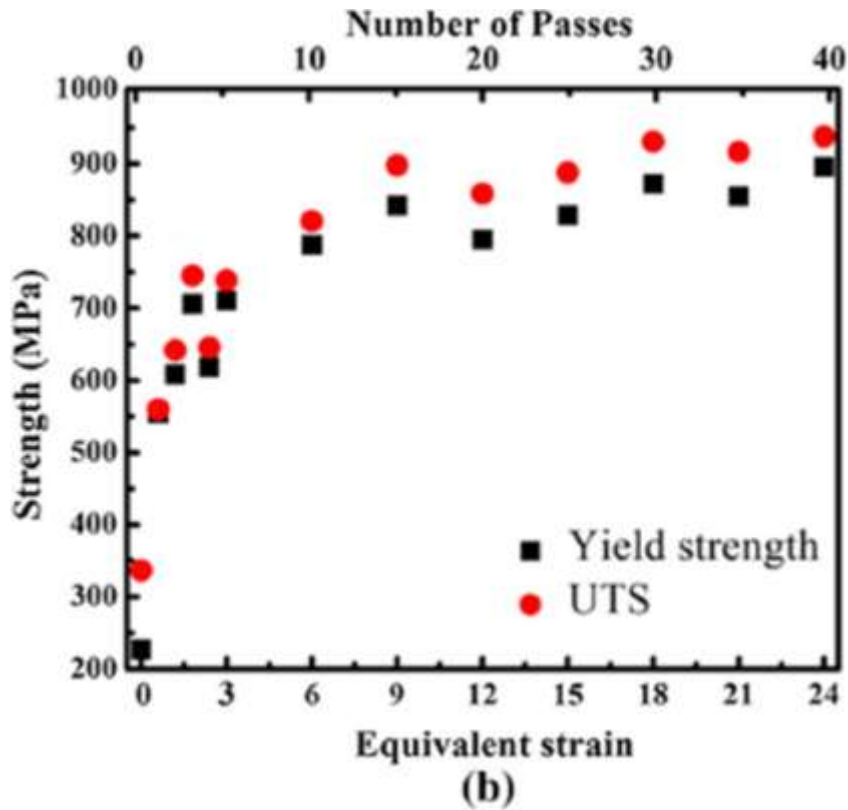
Figure 1.29: Variation of yield strength and ultimate tensile strength with equivalent strain in IF steel deformed by ECAP via route Bc at room temperature [Verma[b] et al. 2016].

Strengthening behavior of low carbon steel has been discussed up to only a maximum equivalent strain of 10 at room temperature [Wang et al.2005] and 12 at 723K [Shin et al. 2003]. Cold-rolling up to 95% reduction in area 95% after eight passes ($\varepsilon_{vm} = 9.2$) of ECAP of IF steel increases the UTS from 689 MPa to 1280 MPa due to further grain refinement, but the total elongation comes down to 3% from 7.3% [Hazra et al. 2010]. Verma et al. [Verma et al. 2017] have also reported that the UTS increases from 859 MPa to 1657 MPa after cold rolling of ECAP-12 up to 90% reduction in area 90% with the reduction in ductility from 16.2 to 2.8%. Increase in strength is due to a reduction in grain size, enhancement in HAGBs fraction and a large number of scattered dislocations. Cryo-rolling of ECAP-12 IF steel up to a

reduction in area of 96% at -50°C increases the dislocation density which results in enhancement of the UTS from 795 MPa to 1409 MPa with the reduction in total elongation from 16.8% to 1.7% [Verma et al. 2017]. Therefore, there is a need to explore the strengthening behavior beyond equivalent strain of 10 by ECAP at room temperature in low carbon steel.

1.7.2 Strain hardening stages in ultrafine-grained material

Strain hardening or strengthening of an SPD processed material can be understood from different stages in flow curve. Strain hardening takes place in polycrystalline materials in various stages due to evolution of different microstructural features at different strain levels. Beygelzimer and Toth have summarised the strengthening behavior of severely deformed commercially pure copper [Beygelzimer et al. 2015]. Figure 1.30 gives the flow curves determined by the authors representing flow stress versus shear strain. Shear strains are calculated from critical shear strain values. They have shown that there are five stages of strengthening for a deformed material and stage-I is absent in UFG polycrystalline copper because it occurs in a single crystal. Strengthening starts with stage-II and is very short stage as the strain ranges from 0 to 0.29. The stage-II is steepest among all the stages of work hardening of the order of $\mu/200$, where μ is the shear modulus, and double slip is taking place. The stage is independent of the material. Stage-III ranges from equivalent strain 0.29 to 0.58 with a decreasing gradient in work hardening. This stage is very sensitive to temperature and rate of deformation. Stage-III strongly depends on the material. It can be described by the power law. At this stage, the slip pattern is multiple slip in the individual crystal.
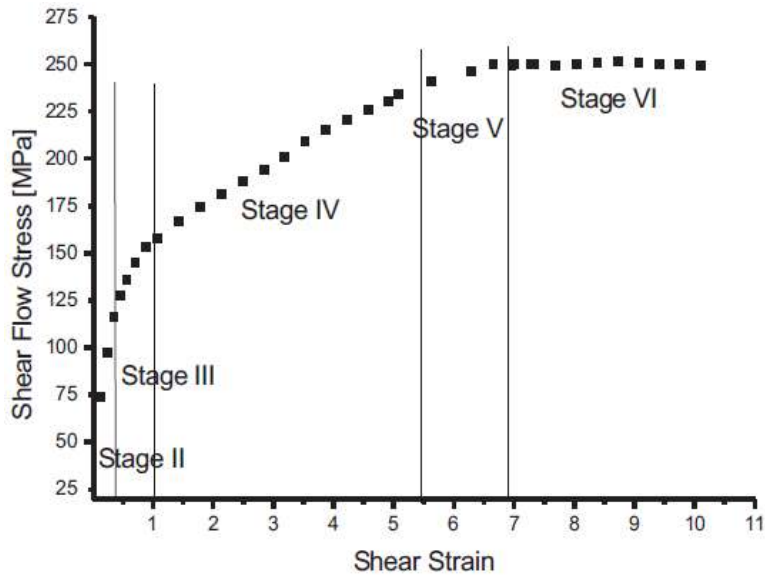
Figure 1.30: Flow curve determined on commercially pure copper in large strain, free-end torsion illustrating the work hardening characteristics of Stages II–VI [Beygelzimer et al. 2015].

Stage-IV is a long linear stage. At this stage shrinking of dislocation cells continues with a progressive sharpening of wall thickness and grain fragmentation. Grain fragmentation process induces progressive build-up of nano subgrain walls, which gradually develop into new subgrain boundaries. In this stage grain fragmentation is the main mechanism which is controlled by the formation of geometrically necessary dislocations. Stage-V is the transition stage between stages IV and VI and it occurs in the equivalent strain range of 3.2 to 4. The concentration of geometrically necessary dislocations (GNDs) decreases in this stage. Above equivalent strain 4 (Stage-VI), GNDs continues to decrease, strain hardening stops, flow stress becomes constant, and grain size reach a saturation level [Beygelzimer et al. 2015].
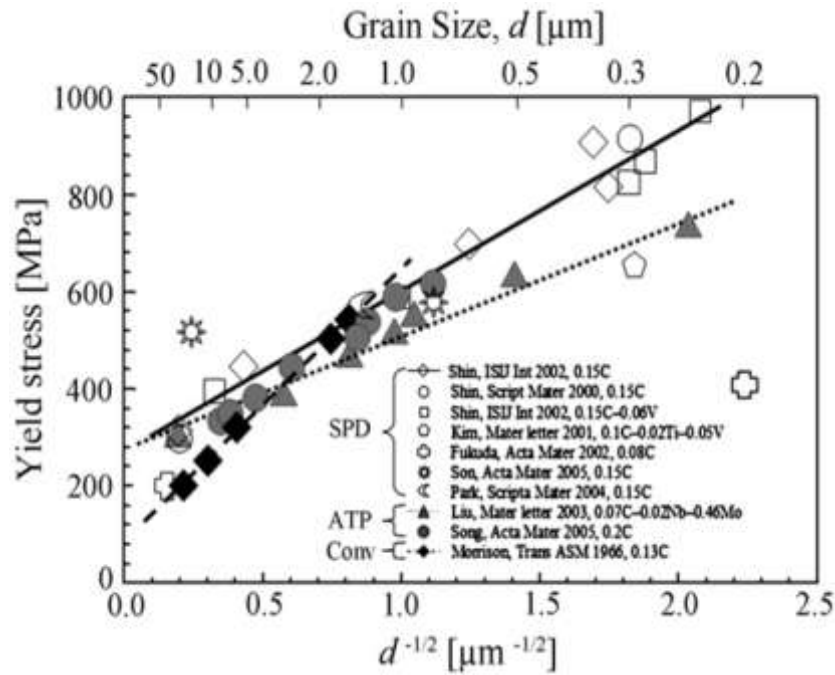
Figure 1.31: Variation of yield strength in low carbon steels with grain size from macrosize to ultrafine size for conventional to severe plastic deformation methods [Song et al. 2006].

Song et al. have summarised the strengthening behavior of low carbon steel as observed by different authors. The yield strength of the material increases as the grain size decreases from micron size range to ultrafine size range (Figure 1.31) [Song et al. 2006].

The enhancement in the strength/hardening is due to (1) refinement of grains, (2) increase in defect density, (3) solid solution strengthening by dissolution of precipitates, and (4) texture hardening strengthening.

1.7.3 Ductility of Ultrafine-Grained Materials

Shin et al. [Shin[a] et al. 2001] have reported that ECAP of 0.2 %C steel for ε_{vm} = 4, the ductility of the material, i.e., total elongation, drops from 33 to 13% due to grain refinement to ultrafine level (0.2 μm) and increase in defect density. ECAP of 0.1wt.% C steel upto an equivalent strain of 3 using route Bc at 150°C results in the

decrease in tensile ductility from 39% to 12% due to the formation of submicrocrystalline grains of the size of 0.3 to 0.6 µm [Kraus et al. 2011]. Fukuda et al. [Fukuda et al. 2002] have deformed 0.08wt.% C steel by ECAP using route Bc at room temperature. Their results show a significant decrease in the elongation to failure due to grain refinement to 0.2 µm. A 0.15wt.% C steel has been deformed through ECAP via route C at 723K upto an equivalent strain of 12 resulting in a decrease in total elongation from 36% to ~12% due to work hardening and grain refinement [Shin et al. 2003]. In the case of an IF steel results show that the microstructure is refined to 0.25 µm, ductility drops to 13.8% from 41.8% due to lack of further work hardening ability of ultrafine-grained microstructure [Verma[b] et al. 2016]. Mechanical properties and grain size of ultrafine-grained low carbon steel produced by SPD processes are summarized in the Table 1.5. The above studies reflect that when the grain size decreases to the ultrafine range in low carbon steels, ductility drops significantly. Loss of ductility in UFG steel is of serious concern for their structural applications of UFG steels.
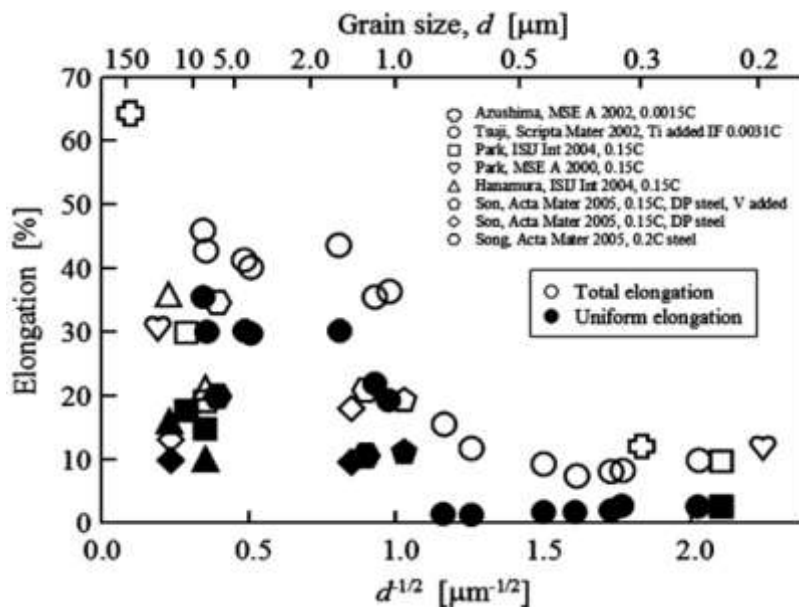

Figure 1.32: Variation of elongation in low carbon steels with grain size from macrosize to ultrafine grain size for conventional to severe plastic deformation methods [Song et al. 2006].

Table 1.5: Mechanical properties and grain refinement details of low carbon steels processed using SPD methods.

Author	Steel (wt.% C)	ECAP Route/ temp (K)	Imposed strain	Grain size (µm)	YS/UTS MPa	TE (%)
Shin[a] et al. 2001	0.15	C/623K	8	0.3		
Shin et al. 2000	0.15	C/623K	4	0.2-0.3		
Fukuda et al. 2002	0.08	Bc/RT	3	0.2	-/>800	4
			2		700	0.3
			1		680	35
Wang et al.2010	0.12	Cold rolling	4		663/788	21.6
Kraus et al 2011	0.1	Bc/150	3	0.3-0.6	552/884,	11.5
		Bc/200	3	0.3-0.6	814/819	9
		Bc/250	3	0.3-0.6	660/780	13.5
		Bc/300	3	0.3-0.6		13
Shin[b] et al.2001	0.2	C/623K	4	0.2	/970	13
Wang et al 2005	0.15	C/RT	10	0.2-0.3	/1200	
Maier et al. 2013	0.09	Bc/573K	3.6	0.32		
Shin et al. 2003	0.15	C/723K	12		950	
Verma[b] et al. 2016	IF steel	Bc/RT	24	0.25	937	13.8

1.8 Fracture behavior of ultrafine-grained material

Fracture behavior of ultrafine-grained material is different as compared to coarse-grained materials. Verma et al. [Verma[b] et al. 2016] have reported the fracture behavior of ultrafine-grained IF steel at low to high strain levels. As the ε_{vm} increases from 0.6 to 6 average dimple size decreases to 24 µm from 60 µm due to the higher stored strain energy. At an equivalent strain range of $\varepsilon_{vm} = 6$ to 9, the elastic stored energy is not changed, and dimple size is also comparable to a reduction in depth of

the dimples. The observed drop in ductility is ascribed to the reduction in depth of the dimples. At $\varepsilon_{vm} = 24$, dimple size decreases further to 15 µm, and the area of cleavage fracture area increases with the equivalent strain ranging from 9 to 24. Tensile fracture behavior of ultrafine-grained Al-Mg alloy produced using cold-rolling and cryo-rolling have been investigated by Yu et al. [Yu et al. 2015]. They have reported that the dimples on the fracture surface are both deeper and more in number for cryo-rolled samples than for cold-rolled samples. This is behavior because of smaller grain size (404 nm) after cryo-rolling and comparatively large grain size (436 nm) after cold-rolling. Saeidi et al. [Saeidi et al. 2014] have subjected an ultrafine-grained dual phase (DP) low carbon steel to intercritical annealing and rolling. On tensile fracture, course-grained DP steel shows course dimples, and the ultrafine-grained DP steel shows fine dimples on fracture surface. The number of dimples per unit area on the fracture surface depends on the number of nucleation sites and plasticity of the material. If many nucleation sites were present, void growth would be limited because of intersecting and linking up of neighboring dimples. So, the final fracture surface appearance consists of many small, shallow dimples. On the other hand, if very few nucleation sites were present in a ductile matrix, there would be a small number of large dimples on the fracture surface. ARB of commercially pure aluminum up to an equivalent strain of 6.4 produces grain size of 360 nm. Tensile fracture shows the ductile behavior in initial material. After ARB process, the samples showed a ductile fracture having dimples, but these dimples were not as deep as those in the initial material. These were shear dimples, and the failure mode was shear ductile rupture [Eizadjou et al. 2009]. Ductile fractures in most materials have a gray fibrous appearance with equiaxed or hemispheroidal dimples [Gabriel et al. 1998, Hertzberg et al. 1989]. This kind of fracture occurs by the nucleation of microvoids, followed by

their growth and coalescence [Hertzberg et al. 1989]. It is clear that the appearance of microvoids on fracture surfaces depends on the state of stress. So, when failure is influenced by shear stress, the voids tend to be elongated and result in the formation of parabolic depressions on the fracture surfaces. Finally, elongated dimples form in the direction of the shear stresses [Hertzberg et al. 1989].

1.9 Recovery of ductility in ultrafine-grained materials

Recovery of ductility with significant strength in the UFG material is the real challenge. There are various possible ways to restore the ductility of UFG/nanocrystalline materials [Koch 2003, Wang et al. 2004, Karmakar et al. 2013], including the following: incorporation of a bimodal (or multimodal) grain size distribution, a mixture of two or multiple phases with varying size and properties, use of nanoscale growth twins in lieu of the nanograins for strengthening, dispersion of nanoparticles and nanoprecipitates, transformation-induced plasticity, twinning-induced plasticity, lowering of dynamic recovery at low temperature (cryogenic temperatures) or dynamic strain rates, improved strain-rate hardening, and synthesis of material that are truly flaw-free materials [Wang and Ma et al. 2004]. Except the first one, all other methods can be applied to a specific alloy only; however, bimodal grain size distribution can be applied to any polycrystalline metallic materials.

Wang et al. rolled copper to 93% reduction in area at liquid nitrogen temperature followed by short annealing at 200°C for 3 minutes. The cold rolling of copper at liquid nitrogen temperature produced nanocrystalline/UFG microstructure of grain size < 200 nm. The yield strength of the material increases by 5 to 6 times that of the coarse-grained counterpart, but ductility decreases to ~23% from 70%. On short annealing above secondary recrystallisation, (ie. at 200°C, for 3 minutes)

material is fully recrystallised followed by secondary recrystallisation. At this stage majority of the grains are in ultrafine range (< 300 nm) with some micron-sized (1-3 µm) grains of ~25% area fraction (Figure 1.33). The yield strength of UFG copper with bimodal grain size distribution is reduced marginally, but ductility is recovered to that of as-received coarse-grained copper (Figure 1.34) [Wang et al. 2002]. Here ultrafine grains maintain strength, but micron size grains add ductility to the material [Wang et al. 2002, 2004, Ma 2003, 2006, Azizi-Alizamini et al. 2007].
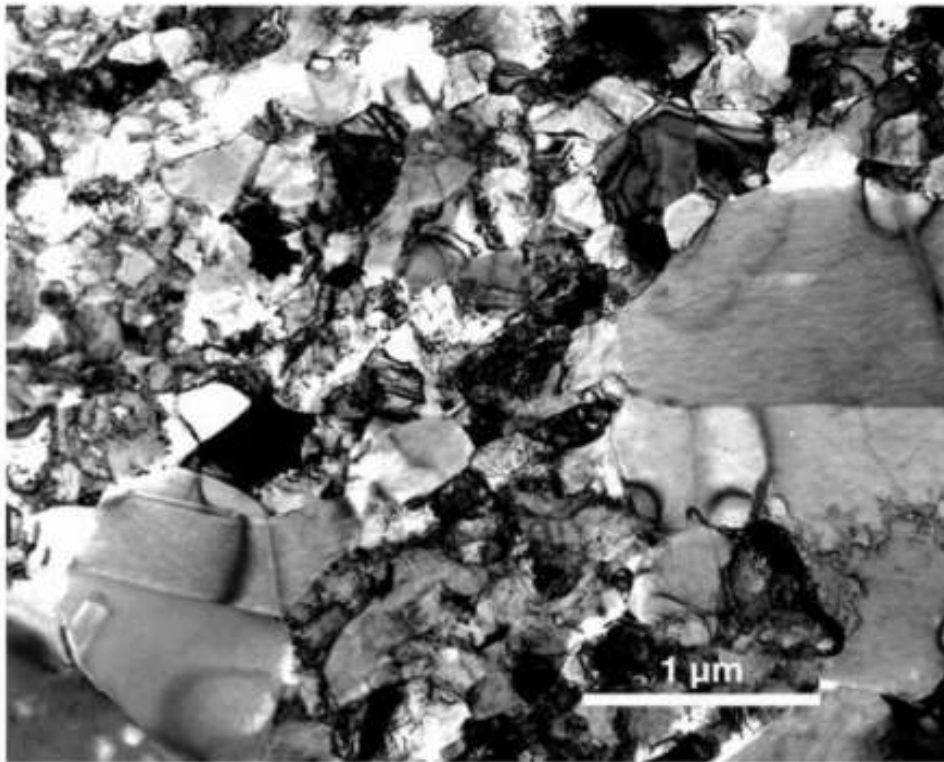

Figure 1.33: Transmission electron micrograph showing grains after secondary recrystallisation that occurred due to after annealing at 200°C for 3 min. The vast majority of the grains are in the nanocrystalline/ultra fine range with some recrystallized regions [Wang et al. 2002].
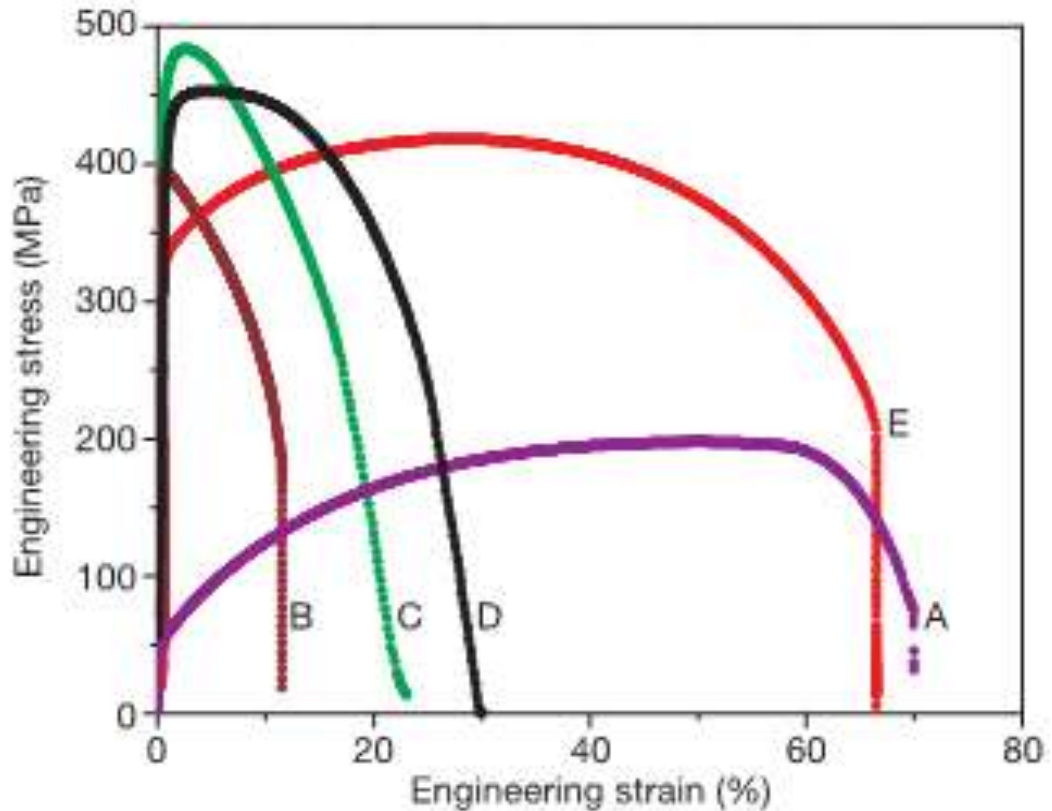
Figure 1.34: Engineering stress–strain curves for pure Cu after annealing at various tempertures. Curve A is for annealed, coarse grained Cu; B for room temperature rolling to 95% cold work (CW); C for liquid-nitrogen temperature rolling to 93% CW; D for 93% CW and annealed at 180°C for 3 min. and E for 93% CW and annealed at 200°C for 3 min [Wang et al. 2002].

The ductility of the material is maximum when the grain size is at 1-10 μm level [Song et al. 2006]. Ductility of Fe-36Ni was recovered with increased strength by annealing of cryo-rolled material from uniform elongation of 3 to 27.4% due to the bimodal distribution in the grain size [Zheng et al. 2016]. The dual-phase microstructure of ferrite and martensite can also provide an excellent combination of strength and ductility. A few attempts are also made to produce bimodal grain size distribution in UFG LCS [Valiev et al. 2006, Shin 2005, Hosseini et al. 2012, Kumar et al. 2011], Therefore, there is a possibility to produce ultra high strength steel by severe plastic deformation due to formation of UFG grains and yet recover ductility

by achieving a bimodal grain size distribution through post ECAP processing and heat treatment.

1.10 Flash annealing: promising microstructure, mechanical properties

Short annealing or flash annealing is a process of heating a material for a short period to enhance nucleation rate of recrystallisation with restricted grain growth. The objective of short annealing or flash annealing is to encourage abnormal grain growth or secondary recrystallisation on material. Secondary recrystallisation becomes easier in diffused-texture material. It happens at high temperature for specific grains in which the ratio of grain boundary energy to average grain boundary energy exceeds 10. Abnormal grain growth is encouraged when second phase particle becomes unstable at high temperature [Humphreys 1994].

Short annealing of deformed martensitic structure in 0.13wt% carbon steel produces recrystallized ferrite of 0.65 µm and the coarse grains of ferrite of ~2.5 µm with precipitation of fine carbide particles of 65 nm. The bimodal grain size distribution of micron to submicron-sized ferrite grains with fine cementite particles offers a good combination of strength (UTS, 810 MPa) and ductility (uniform elongation 16.8%) [Shin[b] et al. 2001].

UFG low carbon steel produced by plane strain compression test at the room temperature is annealed at 600 °C for 120 seconds. Results show that average ferrite grain size is 0.65 µm and UTS is 810 MPa with total elongation 16.8% [Hosseini et al. 2012]. Kumar et al. [Kumar et al. 2011] produced ultrafine grains in 316L stainless steel by cold rolling and short annealing cycles for less than a minute. Verma et al. [Verma et al. 2017] have developed UFG IF steel by ECAP+cold/cryo-rolling. Flash

annealing at 675°C for 5 minutes of UFG IF steel produces a microstructure with increased grain size (from 0.2 μm to 0.6 μm).

1.11 Objectives of Thesis

The present investigation is aimed at the development of bulk ultrafine-grained low carbon steel of high strength and high ductility through equal-channel angular pressing (ECAP) in combination with rolling and thermal treatments. The objectives of the present investigation are

1. Development of bulk ultrafine-grained low carbon steel at large equivalent strain using equal channel angular pressing.

2. Microstructural characterisation of ultrafine grained low carbon steel, exploring mechanism of grain refinement and its correlation with processing parameter.

3. Understanding of texture development in severely deformed low carbon steel.

4. Effects of carbon and dissolution of carbide on microstructural refinement and development of texture.

5. Development of ultra high strength low carbon steel by ECAP. Correlation of mechanical properties of ultrafine-grained low carbon steel with microstructure.

6. Effect of cold-rolling and cry-rolling on microstructure and mechanical properties of ultrafine-grained low carbon steel.

7. The development of bimodal grain size distribution in ultrafine-grained low carbon steel by a combination of severe plastic deformation and suitable post-processing treatments and its impact on mechanical properties.

Finally, a correlation of processing conditions, microstructure, texture and mechanical properties needs to be established.